Available online at www.sciencedirect.com
SCIENCE DIRECT®
Computers & Fluids 35 (2006) 245–279
computers & fluids
www.elsevier.com/locate/compfluid

The normal and oblique collision of a dipole with a no-slip boundary

H.J.H. Clercx [a,*], C.-H. Bruneau [b]

[a] *J.M. Burgers Centre for Fluid Dynamics, Department of Physics, Eindhoven University of Technology, P.O. Box 513, 5600 MB Eindhoven, The Netherlands*
[b] *Mathématiques Appliquées de Bordeaux, Université Bordeaux 1, 351 Cours de la Libération, 33405 Talence Cedex, France*

Received 2 December 2003; received in revised form 23 June 2004; accepted 26 November 2004
Available online 21 April 2005

Abstract

Benchmark results are reported of two separate sets of numerical experiments on the collision of a dipole with a no-slip boundary at several Reynolds numbers. One set of numerical simulations is performed with a finite differences code while the other set concerns simulations conducted with a Chebyshev pseudospectral code. Well-defined initial and boundary conditions are used and the accuracy and convergence of the numerical solutions have been investigated by inspection of several global quantities like the total kinetic energy, the enstrophy and the total angular momentum of the flow, and the vorticity distribution and vorticity flux at the no-slip boundaries. It is found that the collision of the dipole with the no-slip wall and the subsequent flow evolution is dramatically influenced by small-scale vorticity produced during and after the collision process. The trajectories of several coherent vortices are tracked during the simulation and show that in particular underresolved high-amplitude vorticity patches near the no-slip walls are potentially responsible for deteriorating accuracy of the computations in the course of time. Our numerical simulations clearly indicate that it is extremely difficult to obtain mode- or grid-convergence for this seemingly rather simple two-dimensional vortex–wall interaction problem.

PACS: 47.11.+j; 47.32.Cc

* Corresponding author. Tel.: +31 40 247 26 80; fax: +31 40 246 41 51.
E-mail address: h.j.h.clercx@tue.nl (H.J.H. Clercx).

0045-7930/$ - see front matter © 2005 Elsevier Ltd. All rights reserved.
doi:10.1016/j.compfluid.2004.11.009

1. Introduction

Direct numerical simulations (DNS) of two-dimensional (2D) turbulence in bounded domains have recently elucidated the importance of the role of no-slip boundaries in general, and vortex–wall interactions in particular. For example, the evolution of the number of coherent vortices during the decay of 2D turbulence in a container with rigid boundaries is strongly modified by the formation of vortices that originate from thin detached boundary layers [1]. The boundaries thus act as a source of relatively small-scale vortices. In an attempt to quantify the amount of vorticity produced near the no-slip walls Clercx and van Heijst [2] proposed to set up a relatively simple numerical experiment: create a self-propelling dipole in a square container with no-slip walls, that unavoidably moves to one of the boundaries, and analyse the vorticity production in the boundary layers. This study was restricted to the accurate simulation of the primary collision of a dipole with a no-slip wall, and was therefore not extremely CPU and memory demanding as long as the integral-scale Reynolds number $Re = \frac{UW}{\nu} \lesssim 10,000$ (with U and W characteristic velocity and length scales of the flow and ν the kinematic viscosity of the fluid). After the formation of the boundary layers and the subsequent detachment, a complicated sequence of vortex–wall interactions is observed to take place. Such events have been reported already one decade ago by Orlandi [3], but our numerical experiments discussed in the present paper revealed the enormous difficulty to obtain a well-resolved interaction scenario of the dipole with the no-slip wall, usually including a sequence of vortex–vortex and secondary vortex–wall interactions.

The observation that the proposed simple 2D dipole-wall collision experiment represents an extremely tough numerical test case for benchmark purposes, which will be further substantiated in this paper, underlines the need for a better understanding of the relevant physical mechanisms. This is not only important for the relatively simple 2D flows, but also for 3D bounded flows or flows around bluff bodies. Moreover, one should be aware of the possible lack of resolution of the boundary layers in many 3D flows. It should be mentioned, however, that in 2D flows the energy preferably moves from small scales towards large scales (as a result of the inverse energy cascade). Therefore, it might be expected that 2D flows will be more sensitive to small-scale details of the flow and back-scatter phenomena than 3D flows.

The perpendicular dipole-wall collision experiment has also become a test case to investigate the reliability of several numerical codes such as those for 2D incompressible bounded flows and for open 2D flows with obstacles. For example, Ould-Salihi et al. [4] used the dipole-wall collision to validate particle methods against finite-difference methods and Cottet et al. [5] used the dipole as a benchmark to validate mesh adaptation techniques that allow using refined vortex methods in both directions near the wall. The dipole-wall collision has also been used to investigate the performance of a B-spline based numerical method on a zonal embedded grid [6]. The normal dipole-wall collisions in these numerical experiments were conducted at a much more qualitative level than reported in the present paper. In our opinion the dipole-wall collision has, however, never got the status of a mature benchmark experiment, as it should be, to validate quantitatively alternative numerical techniques. A few examples of these techniques, suitable for problems requiring well-resolvedness of the thin boundary layers near no-slip walls, are vortex methods [4,5,7], the recently successfully applied penalisation techniques for finite differences and pseudospectral Navier–Stokes solvers [8,9], and immersed boundary methods [10]. In particular, the accurate prediction of the vorticity produced near these boundaries is found to be essential for the accurate

prediction of vortex trajectories, and the subsequent secondary vortex–wall collisions for example. In this paper we investigate the normal and oblique dipole-wall collision, where the latter one concerns the collision of a dipole with the boundary near one of the corners of the square domain, with two completely different numerical methods that were available 'on-the-shelf' for this purpose: a finite differences scheme using a V-cycles multigrid procedure, and a pseudospectral Chebyshev method. As will be seen, a well-resolved flow evolution[1] beyond the primary dipole-wall collision is found to be extremely CPU and memory demanding despite the simplicity of the flow problem. Benchmark data are provided for a series of numerical experiments, including predictions of the vorticity and vorticity gradients during the interaction process and the vortex trajectories.

2. Numerical methods

The present investigations concern numerical studies of the normal and oblique collision of a dipole with a no-slip wall. The 2D incompressible Navier–Stokes equations have been solved numerically by a finite differences scheme (in the primitive variable formulation) and by a pseudospectral scheme (in the velocity-vorticity formulation).

2.1. Finite differences numerical simulation in primitive variables

We solve the 2D unsteady Navier–Stokes equations written in primitive variables for an incompressible flow in a square domain $\mathscr{D} = (-1,1) \times (-1,1)$ with the no-slip condition at the boundary $\partial\mathscr{D}$. The Cartesian coordinates in a frame of reference are denoted by $\mathbf{x} = (x,y)$. The dimensionless formulation reads

$$\begin{cases} \frac{\partial \mathbf{u}}{\partial t} + (\mathbf{u}\cdot\nabla)\mathbf{u} - \frac{1}{Re}\nabla^2\mathbf{u} + \nabla p = 0 \quad \text{in} \quad \mathscr{D}_T = \mathscr{D}\times(0,T), \\ \nabla\cdot\mathbf{u} = 0 \quad \text{in } \mathscr{D}_T, \\ \mathbf{u}(\cdot,0) = \mathbf{u}_0 \quad \text{in } \mathscr{D}, \\ \mathbf{u} = 0 \quad \text{on } \partial\mathscr{D}_T, \end{cases} \tag{1}$$

where $\mathbf{u} = (u,v)$ and p are the dimensionless velocity and pressure, respectively, $Re = UW/\nu$ is the integral-scale Reynolds number (where U is a characteristic velocity of the flow, W the half width of the domain and ν the kinematic viscosity of the fluid) and $\mathbf{u}_0$ is the initial datum that checks numerically the boundary condition (see Section 3). Time has been made dimensionless by the advection time scale W/U.

The evolution problem is approximated by a second-order Gear scheme with explicit treatment of the convection term,

[1] In other words, and used throughout this paper, mode-convergence when pseudospectral methods with sufficient Chebyshev polynomials in both coordinate directions are used, or grid-convergence when using a sufficiently fine computational grid for the finite differences method.

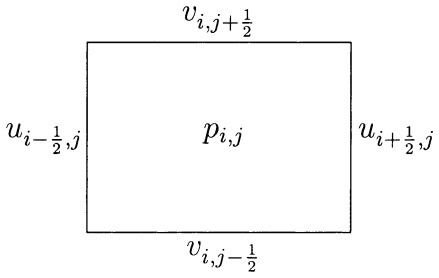

Fig. 1. A staggered cell as used in our finite difference computations (see text for more details).

$$\begin{cases} \frac{3\mathbf{u}^n}{2\Delta t} - \frac{1}{Re}\nabla^2\mathbf{u}^n + \nabla p^n = \frac{4\mathbf{u}^{n-1}-\mathbf{u}^{n-2}}{2\Delta t} - 2(\mathbf{u}^{n-1}\cdot\nabla)\mathbf{u}^{n-1} + (\mathbf{u}^{n-2}\cdot\nabla)\mathbf{u}^{n-2} & \text{in } \mathscr{D}, \\ \nabla\cdot\mathbf{u}^n = 0 & \text{in } \mathscr{D}, \\ \mathbf{u}^n = 0 & \text{on } \partial\mathscr{D}. \end{cases} \tag{2}$$

The use of a second-order scheme is crucial as the first-order Euler scheme for instance does not describe properly the evolution of the solution unless a very low CFL number is used.

The primitive unknowns velocity and pressure are set on staggered grids as illustrated on Fig. 1. The space approximation is then performed using second-order centered finite differences for the linear terms and a third-order upwind Murman scheme for the convection term as described by Bruneau and Saad [11] and Bruneau and Jouron [12]. The schemes are modified at the boundary to better integrate the no-slip condition and keep the second-order accuracy. The location of the unknowns enforce the divergence-free equation which is discretized on the pressure points inside a cell. The equations are solved by a strongly coupled method where the discretized equations in velocity and pressure are solved simultaneously. The pressure is computed directly with the velocity and no correction is needed. As the pressure is known with respect to a constant, it is chosen to shift the pressure field in order to have $p = 0$ at the center $(0,0)$ of the domain. DNS are performed using a V-cycles multigrid algorithm with a cell by cell relaxation procedure as smoother. That means that a 5×5 linear system for the five unknowns of a cell is solved before going to the next cell [11]. The coarsest grid is chosen very coarse (a 4×4 or a 6×6 uniform mesh) in order to get easily the mean flow and a diadic refinement is used to construct the finer grids. A set of nine or ten grids is currently used to solve this problem. As an example we can have a 6×6 grid as grid one, a 12×12 grid as grid two and so on up to a 3072×3072 grid as grid ten which is the finest grid on which we present the results. So when we refer to a 3072×3072 grid solution that means that we have the previous set of grids and when we refer to a 2048×2048 grid solution that means that we have a set of ten grids starting from the coarsest 4×4 grid. In the following we shall refer to a finite differences approximation by giving the number N_{FD} of equidistant cells in each direction on the finest grid; for instance $N_{\mathrm{FD}} = 2048$.

2.2. A 2D pseudospectral Chebyshev method in the $(\boldsymbol{u}, \omega)$ formulation

Pseudospectral simulations were performed with a numerical code developed by Clercx [13]. The pseudospectral scheme is based on an expansion of the flow variables in Chebyshev polynomials, allowing the application to flows in bounded domains with no-slip boundaries. On the domain $\mathscr{D}$, the vorticity problem can be written in the dimensionless form [14]

$$\begin{cases} \frac{\partial \omega}{\partial t} + (\mathbf{u}\cdot\nabla)\omega = \frac{1}{Re}\nabla^2\omega & \text{in } \mathscr{D}_T, \\ \omega(\cdot,0) = \omega_0 & \text{in } \mathscr{D}, \\ \omega = \nabla\times\mathbf{u} & \text{on } \partial\mathscr{D}_T, \end{cases} \tag{3}$$

where $\omega = \partial v/\partial x - \partial u/\partial y$ is the dimensionless (scalar) vorticity and ω_0 the initial datum. The integral-scale Reynolds number is defined as before, $Re = UW/\nu$. The vorticity problem (3) has to be solved in combination with the Poisson problem

$$\begin{cases} \nabla^2\mathbf{u} = \hat{\mathbf{k}}\times\nabla\omega & \text{in } \mathscr{D}_T, \\ \mathbf{u} = 0 & \text{on } \partial\mathscr{D}_T \end{cases} \tag{4}$$

with $\hat{\mathbf{k}}$ the unit vector perpendicular to the plane of the flow. The time discretization of the vorticity equation (3) consists of the second-order explicit Adams–Bashforth scheme for the advection term and the implicit Crank–Nicolson procedure for the diffusion term. Application of this semi-implicit scheme to Eq. (3) yields

$$(\nabla^2 - \lambda)\omega^{n+1} = -(\nabla^2 + \lambda)\omega^n + Re[3(\mathbf{u}\cdot\nabla\omega)^n - (\mathbf{u}\cdot\nabla\omega)^{n-1}] \quad \text{in } \mathscr{D} \tag{5}$$

with $\lambda = 2Re/\Delta t$. Once the new value ω^{n+1} of the vorticity at time step $n+1$ is calculated by means of (5), the Poisson equations for the velocity field are solved straightforwardly: $\nabla^2\mathbf{u}^{n+1} = \hat{\mathbf{k}}\times\nabla\omega^{n+1}$ in $\mathscr{D}$ with $\mathbf{u}^{n+1} = 0$ on $\partial\mathscr{D}$. An alternative discretization scheme, based on a Runga–Kutta procedure, is used for the first time step in order to keep the overall time integration scheme second-order accurate.

The spatial structure of the flow field is approximated by expanding the vorticity and both components of the velocity in a doubly-truncated series of Chebyshev polynomials, for instance:

$$\omega(x,y,t) = \sum_{n=0}^{N}\sum_{m=0}^{M}\hat{\omega}_{nm}(t)T_n(x)T_m(y), \tag{6}$$

where the Chebyshev polynomials T_n are defined as $T_n(x) = \cos(n\theta)$ with $\theta = \cos^{-1}(x)$. On a square domain, it is often appropriate (but not necessary) to choose $M = N$. In the following we shall refer to a pseudospectral approximation by giving the number N_{SM} designating the number of collocation points in each direction on the finest grid; for instance $N_{\mathrm{SM}} = 512$.

All numerical calculations, except the evaluation of the non-linear terms, are performed in spectral space, i.e. the coefficients $\hat{\omega}_{nm}(t)$ and $\hat{\mathbf{u}}_{nm}(t)$ are marched in time. FFT methods are used to evaluate the non-linear terms following the procedure designed by Orszag [15], where the padding technique has been used for de-aliasing. In order to solve Eq. (5), we need to evaluate the boundary values of the vorticity by means of an influence matrix technique [13]. These boundary conditions and those for the Poisson equations of the velocity field are imposed by means of the Lanczos tau method [16].

3. Initial and boundary conditions

Two different dipole-wall collision experiments are considered: a normal collision, i.e. the translation of the dipole being perpendicular to the no-slip wall, and a collision with an angle of

incidence of 30°. Numerical experiments have been conducted with a range of integral-scale Reynolds numbers: $Re = 625$, 1250, 2500 and 5000. The integral-scale Reynolds number is a well-defined number for our simulations, in contrast with Re_d the Reynolds number based on the characteristic velocity and length scale of the dipole, which can only be estimated after the dipole has been formed (around $t = 0.1$). As will be shown later on, for the present runs the two Reynolds numbers are of the same order.

The initial (scalar) vorticity field ω_0 and velocity field $\mathbf{u}_0$ should vanish at the boundary, which guarantees absence of artificial boundary layers due to enforcing the no-slip condition at $t = 0$. In order to satisfy these constraints, two equally strong, oppositely signed, isolated monopoles are put close to each other near the center of the container. The vorticity distribution of the isolated monopoles is chosen as

$$\omega_0 = \omega_e(1 - (r/r_0)^2)\exp(-(r/r_0)^2) \tag{7}$$

with r the distance from the center of the monopole, r_0 its dimensionless 'radius' (at which the vorticity changes sign) and ω_e its dimensionless extremum vorticity value (in $r = 0$). In the present simulations the exact numerical value for the radius of the monopoles is $r_0 = 0.1$, and $\omega_e \approx \pm 320$. With this value of r_0 the vorticity at the boundary (at $r \approx 1$) is virtually zero, as can be concluded by substituting the numerical value of the ratio r/r_0 in Eq. (7).

The value of $\omega_e \approx \pm 320$ is determined by the condition that the total kinetic energy of the dipolar flow field,

$$E(t) = \frac{1}{2}\int_{-1}^{1}\int_{-1}^{1}\mathbf{u}^2(\mathbf{x},t)\,\mathrm{d}x\,\mathrm{d}y, \tag{8}$$

is normalised to $E(0) = 2$ for all runs (or, alternatively, $U = 1/4\int_{\mathscr{D}}\mathbf{u}^2\,\mathrm{d}x\,\mathrm{d}y = 1$). As a consequence, both U and W are fixed and increasing the Reynolds number is achieved by decreasing the kinematic viscosity ν only. The initial total enstrophy of the dipolar flow field,

$$\Omega(t) = \frac{1}{2}\int_{-1}^{1}\int_{-1}^{1}\omega^2(\mathbf{x},t)\,\mathrm{d}x\,\mathrm{d}y, \tag{9}$$

is $\Omega(0) \approx 800$. The exact numerical values for the initial position of the two isolated monopoles is $\{(x_1,y_1), (x_2,y_2)\} = \{(0,0.1), (0,-0.1)\}$ for the normal collision experiment, and $\{(0.0839746, 0.08660254), (0.1839746,-0.08660254)\}$ for the oblique collision experiment. Note that the vortex located at (x_1,y_1) has a positive core vorticity, with $\omega_e \approx 320$, and the vortex located at (x_2,y_2) has $\omega_e \approx -320$. This particular choice of initial positions yields similar collision times t_1 for the first collision of the dipole with the wall ($0.32 \lesssim t_1 \lesssim 0.37$, depending on the Reynolds number) for both sets of numerical experiments.

The initial datum $\mathbf{u}_0 = (u_0, v_0)$ for the integration of the Navier–Stokes equations in primitive variables can be derived straightforwardly for a couple of isolated monopoles, satisfying Eq. (7) and with the vortex centers on $\{(x_1,y_1), (x_2,y_2)\}$, and is then given by

$$\begin{aligned} u_0 &= -\frac{1}{2}|\omega_e|(y-y_1)\exp(-(r_1/r_0)^2) + \frac{1}{2}|\omega_e|(y-y_2)\exp(-(r_2/r_0)^2), \\ v_0 &= -\frac{1}{2}|\omega_e|(x-x_1)\exp(-(r_1/r_0)^2) + \frac{1}{2}|\omega_e|(x-x_2)\exp(-(r_2/r_0)^2) \end{aligned} \tag{10}$$

and $r_1^2 = (x - x_1)^2 + (y - y_1)^2$ and $r_2^2 = (x - x_2)^2 + (y - y_2)^2$. This initial datum also proves that the no-slip condition is sufficiently well guaranteed by our choice $r_0 = 0.1$ (note that $e^{-(r/r_0)^2} \approx e^{-100} \approx 10^{-44}$). For the finite differences simulations the initial pressure is set equal to zero in the whole domain and is updated by the simulation itself within the first iterations. The pseudospectral simulations of the 2D Navier–Stokes equations in the $(\mathbf{u}, \omega)$ formulation are conducted without any reference to a pressure field.

An issue so far untouched is the relation between $Re = \frac{UW}{\nu}$ and $Re_d = \frac{U_d D}{\nu}$, the Reynolds number based on the dipole translation speed U_d and the diameter D of the dipole half. The dipole shown in Fig. 3a can be modelled reasonably well by a Lamb dipole moving with a constant velocity U_d [17]. The stream function distribution $\psi(r, \theta)$, with r and θ representing cylindrical coordinates, for the Lamb dipole is given by

$$\psi(r, \theta) = [2U_d J_1(kr)/kJ_1'(kD)] \sin\theta \quad \text{for } r < D \tag{11}$$

and $\psi(r, \theta) = 0$ for $r \geqslant D$. The function $J_1(kr)$ is the Bessel function of the first kind (and of the first order). Its derivative is denoted by $J_1'(kr) = \frac{dJ_1(kr)}{k\,dr}$. From the definition of Lamb dipole it follows that $J_1(kD) = 0$, or, assuming that the first zero of $J_1(kr)$ should be used, $kD \approx 3.83$. Evaluation of the dimensionless energy and enstrophy yields: $E = \pi\left(\frac{U_d D}{UW}\right)^2$ and $\Omega = \pi(kD)^2\left(\frac{U_d}{U}\right)^2$ (using W and U as characteristic length and velocity scales). Assuming $E = 2$ and $\Omega = 800$ we obtain $\frac{D}{W} \approx 0.19$ and $\frac{U_d}{U} \approx 4.2$, which results in: $Re_d = \frac{U_d D}{UW} Re \approx 0.80 Re$. It is important to note that only an approximate value for Re_d can be found for a moving dipole in a numerical simulation (it is not an exact Lamb dipole), and thus introducing some arbitrariness. Hence we found it preferable to use the well-defined integral-scale Reynolds number Re, even if direct comparison with some literature data [3–5,18] is then not possible.

As an alternative, the Lamb dipole might be used as an initial condition for the simulations. This initial condition should then facilitate a direct comparison with the benchmark simulations reported by Orlandi [3] (although not much numerical data are available from that study for a quantitative comparison). We refrained from conducting this type of numerical experiments. The lack of smoothness of the vorticity field of the Lamb dipole, since the derivative of the vorticity field at the edge $r = D$ of the dipole is discontinuous, might eventually spoil the accuracy of the pseudospectral calculations. Keeping in mind the lack of exhaustive numerical data for benchmark purposes in the literature [3–5,18] the initial conditions for the vorticity and velocity field, based on isolated vortices as introduced in Eqs. (7) and (10), in square bounded domains can in our view serve as the best starting point for extensive benchmark computations.

4. Normal dipole-wall collision

During the last two decades several investigations have been reported on the interaction of a dipole with a boundary. For example, the growth and the eventual separation of a boundary layer due to the (oblique) approach of a vortex pair, in an essentially inviscid flow above a plane no-slip wall, has been studied analytically and numerically by Ersoy and Walker [19]. To our knowledge, the first accurate numerical simulation of 2D vortex dipoles impinging perpendicularly on either a flat no-slip ($\mathbf{u} = 0$ at the wall) or a flat stress-free boundary ($\omega = 0$ at the wall) were reported by Orlandi [3]. These numerical experiments were based on DNS of the

Navier–Stokes equations, thus implying the presence of viscous dissipation away from the flat plate, although the flow above the plate is essentially advection dominated. The Reynolds number in his simulations were $Re_d = 800$, 1600 and 3200 and 256×256 grid points were used in the computations. The following observations were reported for the run with $Re_d = 800$: The primary vortex induces a sheet with high-amplitude opposite vorticity near the flat plate which detaches from the boundary. Subsequently the vorticity filament rolls up and forms a secondary vortex that forms together with the primary vortex an asymmetric dipole. The asymmetric dipole travels with a curved trajectory, first away from the flat plate and later on it approaches the plate again and the primary vortex will collide for the second time with the boundary and produces a tertiary vortex. The secondary vortex is left near the flat plate. The run with $Re_d = 1600$ shows a much more violent vortex–wall interaction, but the scenario resembles the one observed for $Re_d = 800$. However, during the third collision of the primary vortex with the boundary (thus forming a quartiary vortex) the secondary vortex, sitting stationary near the no-slip wall, merges with the tertiary vortex. With its antisymmetric counterpart opposite of the symmetry line (remember that the perpendicular dipole-wall collision is symmetric with respect to the dipole axis) a strong secondary dipole has been formed which is able to escape from the collision region. This dipole moves away from the wall, a distinct difference with the $Re_d = 800$ experiment. A similar numerical experiment with $Re_d = 3200$ revealed persistence of the multiple wall impingement, but the migration of the secondary dipole from the no-slip wall is absent. However, due to the lack of grid-independence it was at that time not clear if the migration of the secondary dipole indeed does not occur.

Similar numerical experiments have been carried out for 2D channel flows by Coutsias and Lynov [18]. They also observed the migration process away from the wall of the secondary dipole, although this time the migration starts directly after the pairing process of the secondary vortices. Similar collision experiments, but now with curved no-slip walls have been presented by Coutsias et al. [20], and by Verzicco et al. [21]. The latter paper concerns an experimental and numerical study of the interaction between a vortex dipole and a circular cylinder.

Recently, the role of no-slip boundaries as an enstrophy source in dipole-wall collisions has been investigated for high Reynolds numbers with DNS in square bounded domains [2]. The Reynolds numbers have been gradually increased up to $Re = 1.6 \times 10^5$ in these numerical experiments, and it was revealed that the enstrophy production nearby the no-slip boundary during the dipole-wall collision is proportional to $\sqrt{Re}$, and is one-to-two-orders of magnitude larger than the enstrophy of the dipole itself. It might be expected that very fine grid spacings near the no-slip wall is essential for a well-resolved DNS of the collision. Indeed, with a fine approximation it is possible to give a realistic scenario as well as a good estimate of the energy dissipation and the enstrophy production during the first collision [2,22]. However, as we shall see in the following, even for medium-range integral-scale Reynolds numbers, an extremely fine discretization is required to describe accurately several consecutive collisions and to get quantitative results for substantially larger integration times, viz $\mathscr{T} \sim 10t_1$, with t_1 the time of the primary and most severe collision.

In this paper, we have conducted a serie of numerical experiments in order to answer the following key question: What is the required resolution, for a certain range of Reynolds numbers, for a well-resolved numerical simulation of the dipole-wall collision? The answer on this question is based on the analysis of the time evolution of $E(t)$, $\Omega(t)$ and the palinstrophy $P(t)$, which is a measure for the vorticity gradients in the flow,

Table 1
An overview of the pseudospectral and finite differences simulations of the normal and oblique dipole-wall collision experiments

	Δt	$Re = 625$	$Re = 1250$	$Re = 2500$	$Re = 5000$
N_{SM}					
128	2.50×10^{-4}	×	×	–	–
192	1.25×10^{-4}	×	–	–	–
256	6.25×10^{-5}	×	×	×	×
384	3.33×10^{-5}	–	×	×	×
512	2.00×10^{-5}	–	–	×	×
640	1.25×10^{-5}	–	–	×	×
N_{FD}					
768	8.00×10^{-5}	×	–	–	–
1024	6.25×10^{-5}	×	×	×	–
1536	4.00×10^{-5}	+	×	×	–
2048	3.13×10^{-5}	–	+	×	×
3072	2.00×10^{-5}	–	–	+	×

The first two columns indicate the resolution (N_{SM} or N_{FD}) and the time step (Δt). The conducted numerical experiments are indicated by a × for both tests and by a + for oblique collision only.

$$P(t) = \frac{1}{2}\int_{-1}^{1}\int_{-1}^{1}(\nabla\omega(\mathbf{x},t))^2\,\mathrm{d}x\,\mathrm{d}y, \tag{12}$$

on the vorticity distributions along the no-slip boundaries (i.e. $\omega|_{\partial\mathscr{D}_T}$) and the vorticity fluxes $\partial\omega/\partial n|_{\partial\mathscr{D}_T}$, with $\partial/\partial n$ denoting the normal derivative with respect to the boundary, and on the detailed vortex trajectories before, and more importantly, after the primary collision. The numerical experiments that have been conducted are summarized in Table 1.

The time steps for the pseudospectral runs, shown in Table 1, were chosen to be $\Delta t \approx 9/(2N_{SM}^2)$ (satisfying the stability limit $\Delta t \lesssim 9/N_{SM}^2$ [16]) for $N_{SM} \leqslant 384$. We have relaxed this condition somewhat for the runs with $N_{SM} = 512$ and 640 to reduce the total computation time of the runs, and the lack of scaling with the minimal grid-spacing for high resolutions has thus no special significance (still $\Delta t \lesssim 9/N_{SM}^2$).

Inspection of the time evolution of $E(t), \Omega(t)$ and $P(t)$ for $t \leqslant 2$ revealed the following estimates for the minimum resolution for mode-convergence: $N_{SM} = 256$ for $Re = 625$, $N_{SM} = 384$ for $Re = 1250$, and $N_{SM} = 512$ for $Re = 2500$. The data for the runs with $Re = 5000$ indicate that mode-convergence is not easily obtained. We found that a minimum resolution of $N_{SM} = 640$ is necessary to obtain a mode-convergence up to $t \approx 0.75$ only. For $t \gtrsim 0.75$ the difference between the data obtained for $N_{SM} = 512$ and $N_{SM} = 640$ start to diverge considerably. This indicates that initially small-scale flow features, produced during intense vortex–wall interactions, are not fully resolved yet. Although this does not appreciably affect the flow evolution for $t \lesssim 0.75$, the inverse energy cascade and back-scatter phenomena characteristic for 2D flows eventually yields a slightly modified flow evolution in course of time (as shown by the pseudospectral runs with $N_{SM} = 512$ and 640). The well-resolved simulations for $Re = 625$–2500 indicates that mode-convergence might be achieved for the run with $Re = 5000$ when $N_{SM} \approx 768$. However, the computational costs keeps us from conducting these simulations. The present observations for the resolutions

associated with mode-convergence for simulations of dipole-wall collisions is rather disappointing. We expected initially that a substantially smaller number of Chebyshev polynomials would suffice, because the grid spacing normal to the boundary is inversely proportional to the total number of degrees of freedom, N_{SM}^2. For an equidistant finite differences grid the grid spacing is only inversely proportional to N_{FD}, the number of grid cells per coordinate direction. Grid-convergence for short-time runs (up to $t = 1$) is found to occur with $N_{\mathrm{FD}} = 1024$ for $Re = 625$, $N_{\mathrm{FD}} = 1536$ for $Re = 1250$, $N_{\mathrm{FD}} = 2048$ for $Re = 2500$, and $N_{\mathrm{FD}} = 3072$ for $Re = 5000$. This resolution appears to be consistent with the thickness of the boundary layer. A posteriori estimates of the boundary layer thickness δ, based on the ratio $\omega|_{\partial\mathscr{D}_T}/(\partial\omega/\partial n|_{\partial\mathscr{D}_T})$ indicates that $\delta \approx \frac{1}{4\sqrt{Re}}$ (for example, $\delta_{Re=625} \approx 0.01$ and $\delta_{Re=2500} \approx 0.005$). These results show that the mesh size has to be five times smaller than the (estimated) boundary layer thickness to achieve grid-convergence. With the collocation points it is a little bit less clear as the grid is non-uniform and for an accurate approximation of small-scale vortices and vorticity filaments aligned perpendicularly to the no-slip wall a small mesh size might be necessary in each direction. This condition is not always completely fulfilled. The observation that the need of grid refinement is not exclusively in the direction normal to the wall in turbulent flows is not new; it has long been recognized in the CFD community, see, for instance, Refs. [6,23].

In Fig. 2a we have plotted $E(t)$ for the runs with $Re = 2500$. The data from the simulations with $N_{\mathrm{SM}} = 384$, 512 and 640 collapse onto one curve.[2] The data obtained for the run with $N_{\mathrm{SM}} = 256$ shows a somewhat faster dissipation of kinetic energy which becomes visible for $t \gtrsim 0.8$, and is a result from a slightly different flow evolution. The sharp decrease of $E(t)$ at $t \approx 0.33$ is due to a strong dissipation when the dipole collides with the no-slip boundary. A second collision occurs for $t \approx 0.61$ where again an increased dissipation can be observed. In Fig. 2b we have plotted $\Omega(t)$ for the same set of runs. All data for $N_{\mathrm{SM}} \geqslant 384$ collapse onto one curve, but not surprisingly the enstrophy evolution for the run with $N_{\mathrm{SM}} = 256$ clearly shows an enhanced enstrophy (and an increased dissipation via $\frac{\mathrm{d}E(t)}{\mathrm{d}t} = -\frac{2}{Re}\Omega(t)$) during the final stage of the computed flow evolution. Note that the two enstrophy peaks at $t \approx 0.33$ and 0.61 signals the first and second collision of the primary vortices with the boundary. To illustrate the flow evolution we have plotted a sequence of vorticity contour plots in Fig. 3 clearly showing the production of small-scale vorticity patches, and the migration of a secondary vortex dipole. In Fig. 4 we have plotted vorticity contours for the final stage (at $t = 2$) of our simulation with $Re = 2500$. In (a) we show the final stage for the run with $N_{\mathrm{SM}} = 256$ and in (b) for the run with $N_{\mathrm{SM}} = 640$ (which is also representative for the simulations with $N_{\mathrm{SM}} = 384$ and 512). The different migration process of secondary dipoles is apparent. The same grid-converged solution is obtained with finite differences ($N_{\mathrm{FD}} = 2048$) and a similar change in flow behaviour is observed when changing the resolution from $N_{\mathrm{FD}} = 1024$ to $N_{\mathrm{FD}} = 2048$, indicating that $N_{\mathrm{FD}} = 1024$ results in a too coarse mesh for the present simulation.

The vorticity profiles at the boundary $x = 1$ and the vorticity flux, i.e. the normal derivative of the vorticity, at the boundary $x = 1$ (both shown for $-0.6 \leqslant y \leqslant 0$) are plotted in Figs. 5 and 6 for the runs with $Re = 625$ ($N_{\mathrm{SM}} = 256$), 1250 ($N_{\mathrm{SM}} = 384$), and 2500 ($N_{\mathrm{SM}} = 640$). The data represent

[2] Note that $N_{\mathrm{SM}} = 384$, 512, and 640 correspond to expansions with 385, 513, and 641 Chebyshev polynomials per coordinate direction, respectively.

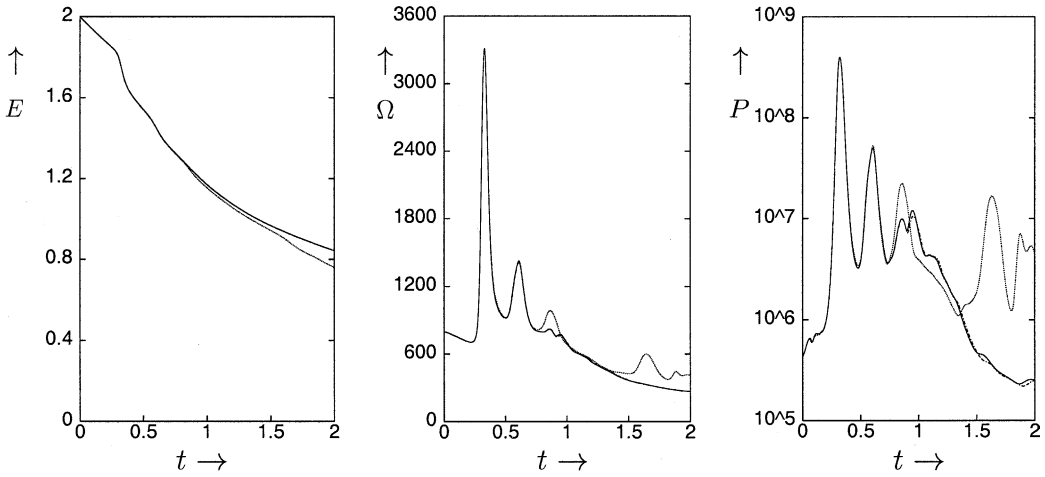

Fig. 2. From left to right: (a) the kinetic energy $E(t)$, (b) the enstrophy $\Omega(t)$, and (c) the palinstrophy $P(t)$ for the normal dipole-wall collision with $Re = 2500$ and different resolutions $N_{SM} = 256$ (dotted), $N_{SM} = 384$ (dashed), and $N_{SM} = 640$ (solid) of the pseudospectral simulations.

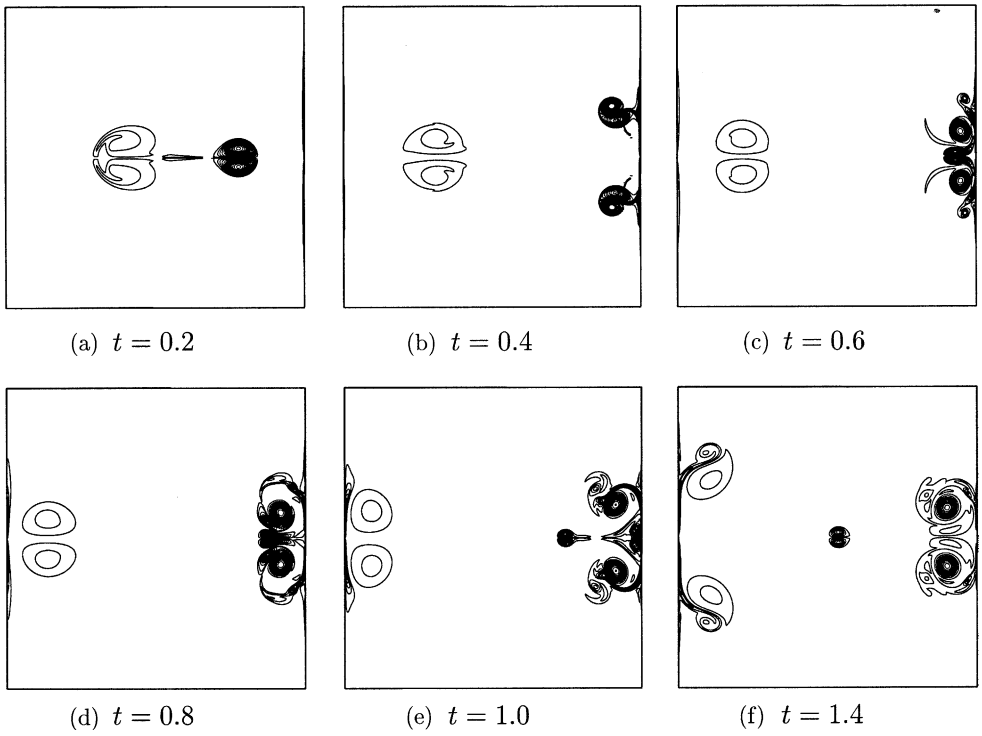

Fig. 3. Vorticity contour plots of the normal dipole-wall collision experiment with $Re = 2500$. The pseudospectral simulations are performed with a resolution $N_{SM} = 640$. The contour levels are drawn for $\ldots, -50, -30, -10, 10, 30, 50, \ldots$ (representing dimensionless vorticity values).

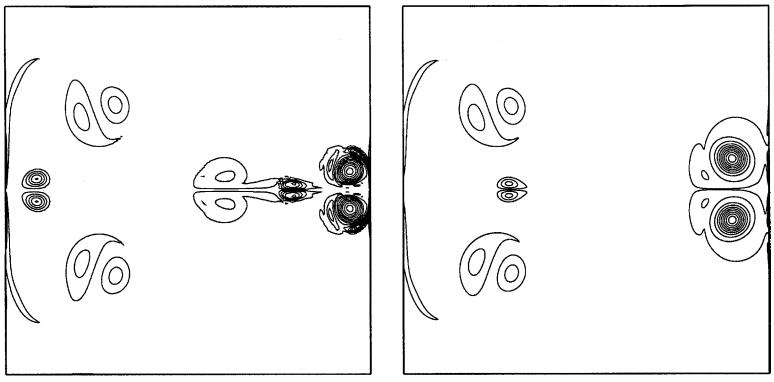

(a) $N_{SM} = 256,\ t = 2.0$ (b) $N_{SM} = 640,\ t = 2.0$

Fig. 4. Comparison of the vorticity contour plots of the normal dipole-wall collision experiment for an underresolved and a well-resolved simulation with $Re = 2500$. The pseudospectral simulations are performed with a resolution $N_{SM} = 256$ (left) and $N_{SM} = 640$ (right). The contour levels are drawn for $\ldots, -50, -30, -10, 10, 30, 50, \ldots$ (representing dimensionless vorticity values).

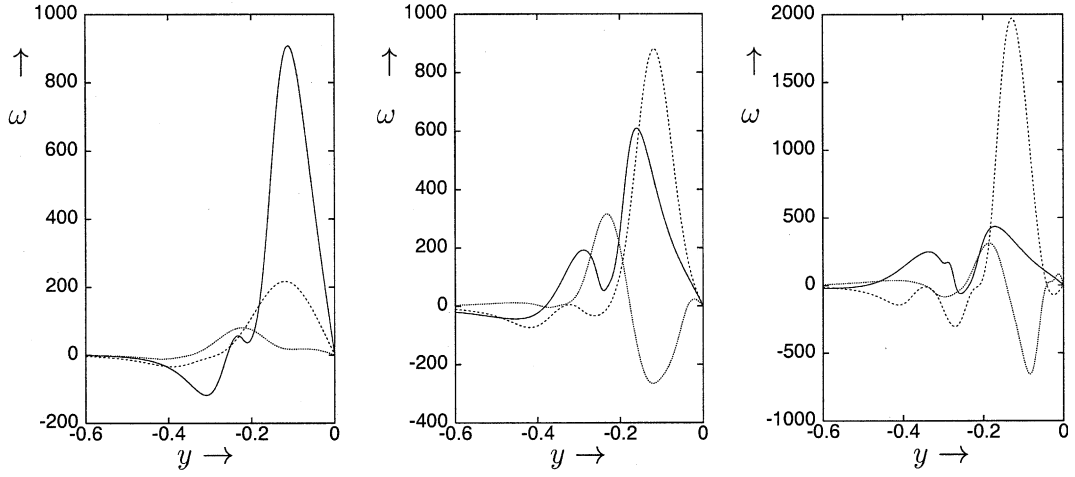

(a) $Re = 625$ (b) $Re = 1250$ (c) $Re = 2500$

Fig. 5. Vorticity at the boundary $x = 1$ for $t = 0.4$ (solid), $t = 0.6$ (dashed) and $t = 1.0$ (dotted) for the normal dipole-wall collision experiment from pseudospectral simulations. The resolution for the different runs is: (a) $N_{SM} = 256$, (b) $N_{SM} = 384$, and (c) $N_{SM} = 640$.

the vorticity and the vorticity flux at the boundary for $t = 0.4$ (solid), 0.6 (dashed) and 1.0 (dotted). The vorticity distributions and the normal vorticity gradients at the boundary are well-resolved; no changes were observed when the resolution was increased further. This is consistent with the results from the finite differences calculations that show the same vorticity distributions at the boundary (for the finest grid solutions) for the simulations with $Re = 625$, 1250 and 2500. The vorticity flux from finite differences calculations shows similar distributions at the boundary,

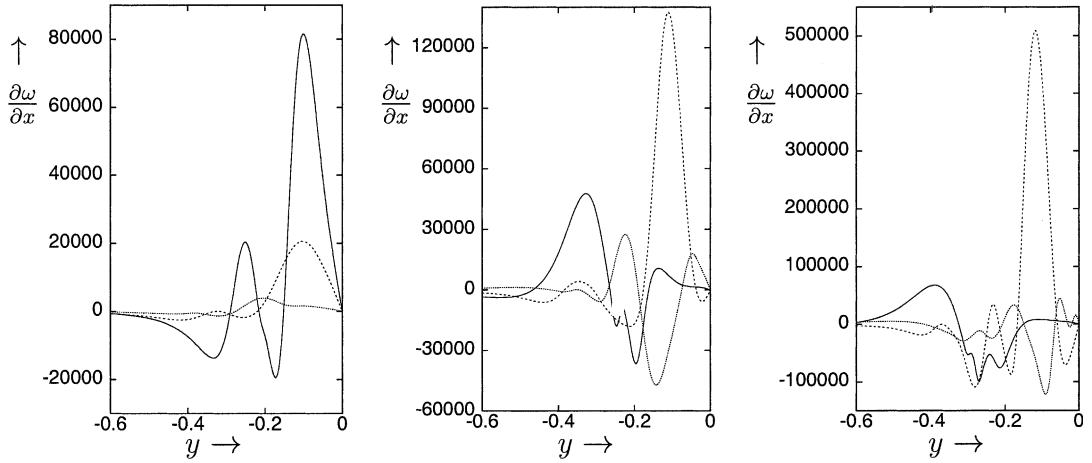

Fig. 6. Vorticity flux at the boundary $x = 1$ for $t = 0.4$ (solid), $t = 0.6$ (dashed) and $t = 1.0$ (dotted) for the normal dipole-wall collision experiment from pseudospectral simulations. The resolution for the different runs is: (a) $N_{SM} = 256$, (b) $N_{SM} = 384$, and (c) $N_{SM} = 640$.

but the computed extrema are found to be less pronounced due to the a posteriori computation of vorticity gradients on a grid that is coarse compared to the spectral collocation grid.

In Tables 2 and 3 we have summarized the value of the first two maxima of $\Omega(t)$ and $P(t)$, respectively, and the times at which these maxima occur (t_1 and t_2 denote the first and second maximum, respectively) for the runs with $Re = 625$, 1250, 2500, and 5000. These data are obtained from the well-resolved simulations based on both the finite differences (FD) and the spectral (SM) computations. For both simulations the highest values of N_{SM} or N_{FD}, as indicated in Table 1, are used. Let us point out to the reader that the vorticity is not an unknown in the FD simulations

Table 2
A summary of the values of the first two maxima of the enstrophy for the normal collision experiment, which occur at t_1 and t_2, respectively

Re	Method	t_1	$\Omega(t_1)$	t_2	$\Omega(t_2)$
625	SM	0.3711	933.6	0.6479	305.2
	FD	0.371	932.8	0.647	305.2
1250	SM	0.3414	1899	0.6162	725.3
	FD	0.341	1891	0.616	724.9
2500	SM	0.3279	3313	0.6089	1418
	FD	0.328	3270	0.608	1408
5000	SM	0.3234	5536	0.6035	3733
	FD	0.323	5435	0.605	3667

SM and FD denote spectral method and finite differences, respectively.

Table 3
A summary of the values of the first two maxima of the palinstrophy for the normal collision experiment, which occur at t_1 and t_2, respectively

Re	Method	t_1	$P(t_1)$	t_2	$P(t_2)$
625	SM	0.3624	1.386×10^7	0.6521	6.777×10^5
	FD	0.363	1.296×10^7	0.653	6.561×10^5
1250	SM	0.3326	8.710×10^7	0.6234	7.159×10^6
	FD	0.333	7.744×10^7	0.623	6.739×10^6
2500	SM	0.3195	3.968×10^8	0.6046	5.021×10^7
	FD	0.320	3.285×10^8	0.604	4.431×10^7
5000	SM	0.3219	1.778×10^9	0.5992	1.04×10^9
	FD	0.322	1.397×10^9	0.601	8.102×10^8

SM and FD denote spectral method and finite differences, respectively.

and is computed a posteriori at the vertices of the meshes by a second-order centered scheme. Consequently, the computation of the palinstrophy requires a double approximation to compute the gradients that is not straightforward and could smooth the function.

The formation of secondary dipoles as reported by Orlandi [3] occurs for a certain range of Reynolds numbers. As can be observed in Fig. 7, where vorticity contour plots are shown for the flow at $t = 1$ for runs with $Re = 625$, 1250, 2500, and 5000, it occurred for the run with $Re = 2500$ only. (Here, only a small part of the computational domain has been shown, $0.4 \leqslant x \leqslant 1$ and $0 \leqslant y \leqslant 0.6$, where we evidently employed the symmetry of the present normal dipole-wall collision experiment.) Indeed as can be seen on Fig. 3, when the initial dipole collides into the wall it produces two symmetric dipoles that turn round and collide again into the wall. According to their distance at the second collision, the dipoles can behave like a rolling-mill and produce a new dipole that is ejected away. That is the case at $Re = 2500$ whereas for $Re = 5000$ the dipoles are too far away from each other to interact. The vorticity contours computed with the finite differences method are identical to those obtained with the spectral method, but we can take benefit of the use of the primitive variables to plot the pressure to see the correlation between the two quantities (Fig. 8).

By analysing the trajectories and vortex strengths of the primary vortices (the two vortices constituting the dipole before the collision with the wall) we can draw a few conclusions. In Fig. 9a we have shown the y-position of the primary vortex (with positive vorticity) as function of the dimension-less time t, and in Fig. 9b the x-position is depicted. The x-coordinate of the primary vortex indicates that for higher Reynolds number the vortex core approaches the boundary more closely, but the distance from the boundary after the first collision depends hardly on the Reynolds number (except for the low-Reynolds number experiment where the vortex core drifts away from the boundary). The y-coordinate of the primary vortex after the first collision shows distinctly different behaviour. The $Re = 625$ and 1250 experiments show similar evolution of the y-coordinate of the vortex position, and thus similar primary vortex trajectories. The formation of a secondary vortex pair after the vortex–wall collision in the simulation with $Re = 2500$ results in a decreasing primary vortex separation in course of time (open squares in Fig. 9). Apparently, the removal of boundary layer vorticity enables the primary vortex cores to approach each other. The run with

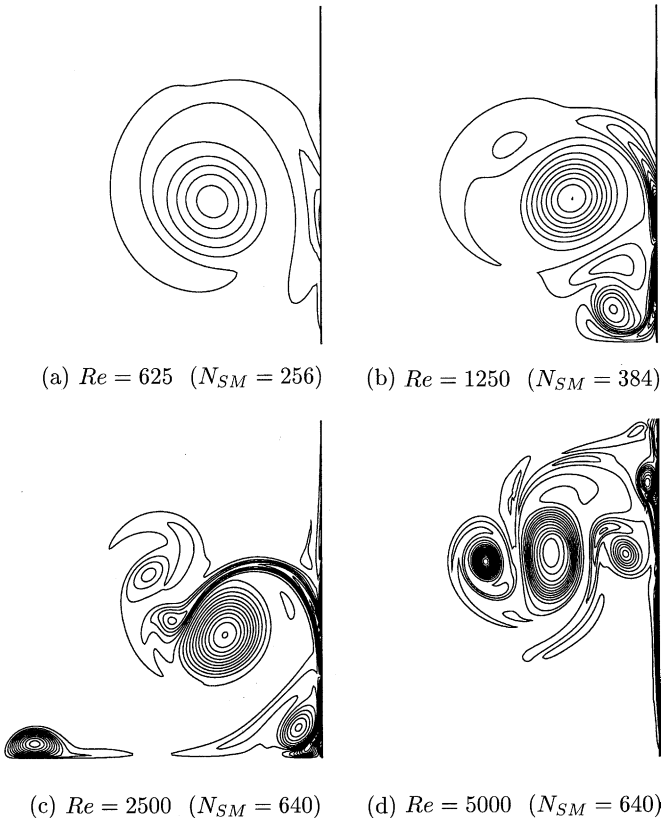

Fig. 7. Vorticity contour plots of the normal dipole-wall collision experiment at $t = 1$ with $Re = 625$ (a), 1250 (b), 2500 (c), and 5000 (d). Only a small part of the computational domain has been shown: $0.4 \leqslant x \leqslant 1$ and $0 \leqslant y \leqslant 0.6$. The pseudospectral simulations are performed with a resolution $N_{\mathrm{SM}} = 256$, 384, 640, and 640, respectively. The contour levels are drawn for $\ldots, -50, -30, -10, 10, 30, 50, \ldots$ (representing dimensionless vorticity values).

$Re = 5000$ shows separation of the primary vortex cores (filled circles in Fig. 9). No vigorous interaction between secondary and tertiary vortices will occur, and no secondary dipole will be formed which travels away from the right boundary. We have also measured the maximum vorticity $\omega_{\max}$ in the (positive) primary vortex. It decays approximately exponentially in course of time, but no appreciable effects are found that are directly a result of the vortex–wall interaction. In particular, a more vigorous vortex–wall interaction for the runs with higher Reynolds number does not automatically lead to enhanced vorticity dissipation in the core of the primary vortices. It is even possible to collect all data reasonably well on a master curve by suitably rescaling time, taking into account the viscous decay.

Finally, we have collected some numerical data which might be used for benchmarking purposes. These data are obtained from the well-resolved simulations (highest values of N_{SM} and N_{FD} as indicated in Table 1). In Table 4 are given the primary vortex position and vortex strength $\omega_{\max}$ at different times. We provide also for the finite differences simulations the pressure at the core of the primary vortex. Let us note that the pressure is shifted in such a way that it is kept

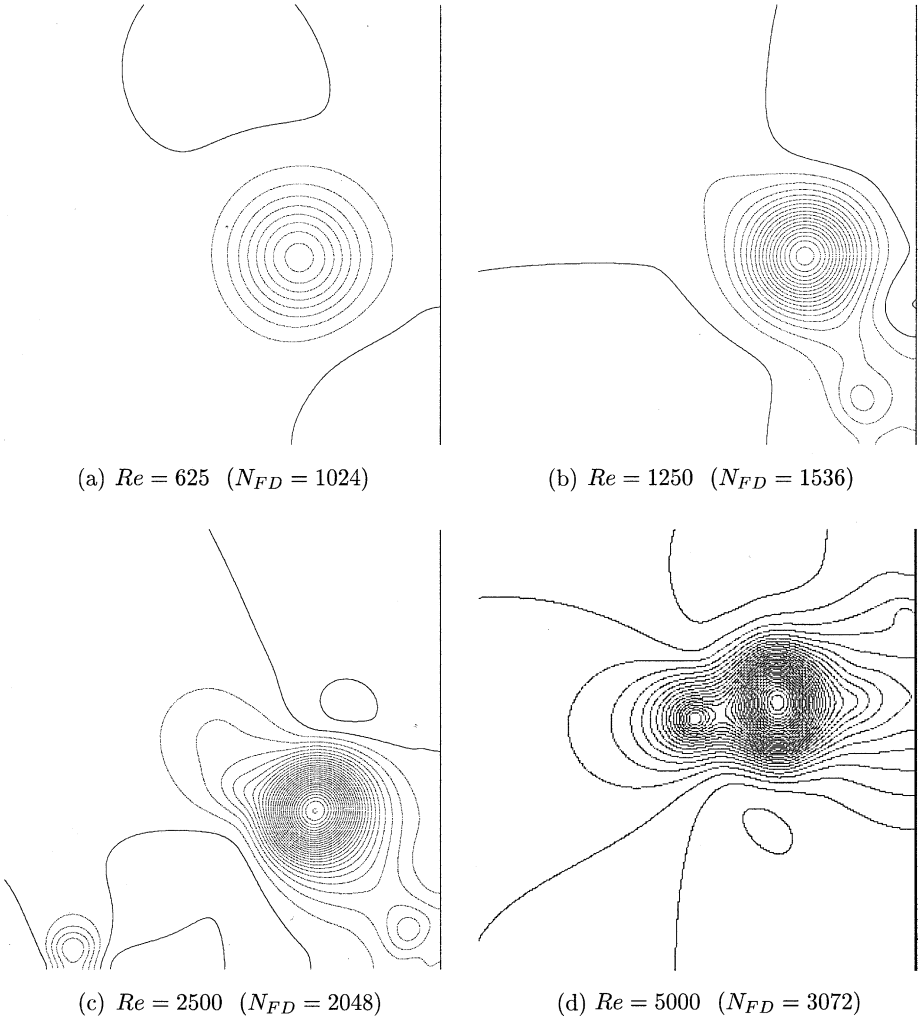

Fig. 8. Pressure contour plots of the normal dipole-wall collision experiment in the window $(0.4,1) \times (0,0.6)$ at $t = 1$ with $Re = 625$ (a), 1250 (b), 2500 (c), and 5000 (d). The finite difference simulations are performed with a resolution $N_{\mathrm{FD}} = 1024$, 1536, 2048, and 3072, respectively. The contour levels are drawn for $\ldots, -3, -2, -1, 0, 1, 2, 3, \ldots$ and the contour line 0 goes through the origin of the domain.

equal to zero at the origin of the domain. The pseudospectral runs with $Re = 5000$ are slightly contaminated by residual high-frequency oscillations. These are due to slight under-resolvedness of the details of the boundary layer formed during the first (and undoubtedly strongest) vortex–wall interaction, and this affects accurate determination of the position and strength of the primary vortices. The data from the finite differences runs are based on previously performed numerical experiments, that were conducted up to $t = 1$. Moreover, no vorticity data were available for $t = 0.6$ [22]. In Table 5 we have summarized the computed values of the global quantities $E(t)$, $\Omega(t)$, and $P(t)$ at $t = 0.25$, 0.50, and 0.75, thus before, in between, and after the first two col-

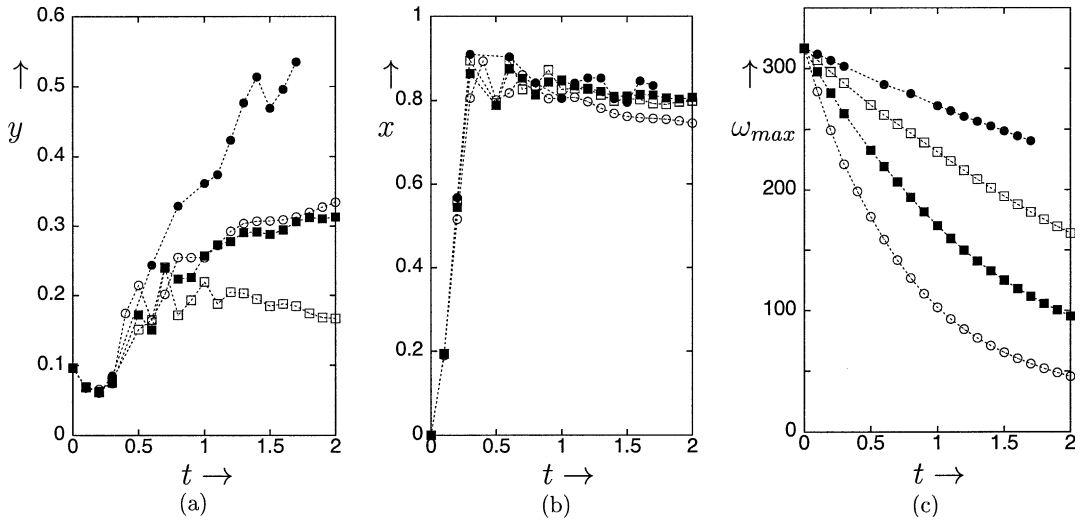

Fig. 9. The trajectory and amplitude of the primary (positive) vortex as function of time. The y-position is displayed in (a), the x-position in (b), and the vortex amplitude in (c). Data are shown for $Re = 625$ (open circles), 1250 (filled squares), 2500 (open squares), and 5000 (filled circles).

Table 4
An overview of the x- and y-coordinate, the maximum strength $\omega_{\max}$ and the pressure p_{FD} at this maximum of the positive primary vortex for different times $t = 0.6$, 0.625, 1.0 and 1.4

Re	t	$(x,y)_{\mathrm{SM}}$	$(x,y)_{\mathrm{FD}}$	$\omega_{\max,\mathrm{SM}}$	$\omega_{\max,\mathrm{FD}}$	p_{FD}
625	0.6	(0.818, 0.165)	–	158.9	–	–
	0.625	–	(0.832, 0.166)	–	154.2	−14.57
	1.0	(0.805, 0.254)	(0.805, 0.254)	102.6	102.6	−8.48
	1.4	(0.769, 0.307)	–	71.0	–	–
1250	0.6	(0.874, 0.151)	–	219.4	–	–
	0.625	–	(0.885, 0.174)	–	216.1	−26.86
	1.0	(0.848, 0.257)	(0.848, 0.258)	170.3	170.3	−17.53
	1.4	(0.809, 0.292)	–	132.7	–	–
2500	0.6	(0.896, 0.165)	–	261.9	–	–
	0.625	–	(0.896, 0.199)	–	260.0	−34.81
	1.0	(0.826, 0.219)	(0.826, 0.217)	231.4	231.4	−27.05
	1.4	(0.798, 0.195)	–	201.6	–	–
5000	0.6	(0.903, 0.244)	–	286.9	–	–
	0.625	–	(0.884, 0.275)	–	285.9	−39.37
	1.0	(0.811, 0.366)	(0.811, 0.367)	269.1	268.6	−29.60

SM and FD indicate spectral method and finite differences, respectively (the pressure is shifted so that $p = 0$ at the origin of the domain).

lisions (at t_1 and t_2, respectively) of the dipole with the no-slip wall. This table allows to quantify in particular the energy dissipation before the first collision with respect to the Reynolds number.

Table 5
A summary of the values of the global quantities for the normal collision experiment at times $t = 0.25$, $t = 0.50$ and $t = 0.75$

Re	t	$E_{SM}(t)$	$\Omega_{SM}(t)$	$P_{SM}(t)$	$E_{FD}(t)$	$\Omega_{FD}(t)$	$P_{FD}(t)$
625	0.25	1.5022	472.6	3.99×10^5	1.502	472.7	3.91×10^5
	0.50	1.0130	380.6	5.53×10^5	1.013	380.4	5.49×10^5
	0.75	0.7673	255.2	4.87×10^5	0.767	255.0	4.73×10^5
1250	0.25	1.7209	615.0	1.13×10^6	1.721	615.0	1.04×10^6
	0.50	1.3132	611.9	1.32×10^6	1.313	611.3	1.29×10^6
	0.75	1.0613	484.7	1.66×10^6	1.061	484.4	1.60×10^6
2500	0.25	1.8509	728.2	4.22×10^6	1.851	727.8	3.52×10^6
	0.50	1.5416	920.5	3.83×10^6	1.541	916.6	3.56×10^6
	0.75	1.3262	808.1	3.79×10^6	1.326	805.5	3.56×10^6
5000	0.25	1.9225	823.1	1.57×10^7	1.923	822.8	1.29×10^7
	0.50	1.6924	1340	1.56×10^7	1.692	1328	1.35×10^7
	0.75	1.4980	1517	1.95×10^8	1.495	1659	1.86×10^8

Reference values at time $t = 0$ are $E = 2$, $\Omega = 800$ and $P = 4.42 \times 10^5$. The indices SM and FD denote spectral method and finite differences, respectively.

5. Oblique dipole-wall collision

Besides the traditional normal dipole-wall collision experiment we have conducted numerical experiments of an oblique dipole-wall collision. The initial trajectory of the dipole has an angle of 30° with the positive x-axis, and collides with the no-slip boundary at $x = 1$ and $y \approx 0.5$ (the collision time is similar as in the previous section: $0.32 \lesssim t \lesssim 0.37$, with $t \approx 0.32$ for the high Reynolds number cases). After the first collision the primary vortex with positive circulation interacts with both the right (at $x = 1$) and the upper (at $y = 1$) no-slip boundary. As an illustration of the flow evolution we show in Figs. 10 and 11 some snapshots of vorticity and pressure contours of runs conducted at $Re = 2500$ with the spectral method ($N_{SM} = 640$) and the finite differences method ($N_{FD} = 3072$). Both methods give exactly the same solution.

The numerical study of the oblique dipole-wall collision revealed again that an extremely large number of Chebyshev polynomials or a very dense grid have to be used in order to obtain mode-convergence or grid-convergence for the dipole-wall collision and its subsequent evolution (see Table 1). The time evolution of the global quantities such as $E(t)$, $\Omega(t)$ and $P(t)$ can be predicted with high accuracy up to $t = 6$ (we did not extend our simulations to $t > 6$) for $Re = 625$ ($N_{SM} = 256$, $N_{FD} = 1536$) and 1250 ($N_{SM} = 384$, $N_{FD} = 2048$). The remnants of the dipole with $Re = 2500$ has fully been captured up to $t \approx 3$ in a simulation with $N_{SM} = 640$ or $N_{FD} = 3072$. However, it appeared to be much more difficult to obtain mode-convergence or grid-convergence for the runs with $Re = 5000$, mainly due to the large fragmentation of the primary dipole after the collision. Reliable converged results are obtained for $t \lesssim 0.8$ for both methods, although we expect that the numerical data from our experiments with $N_{SM} = 640$ are sufficiently converged for $t \lesssim 1.2$. To illustrate the flow evolution for these four different cases we have plotted in Figs. 12 and 13 the vorticity contours, and in Fig. 14 the pressure contours (for the finite differences calculations only) obtained after the collision of the dipole with the wall (the snapshots are taken

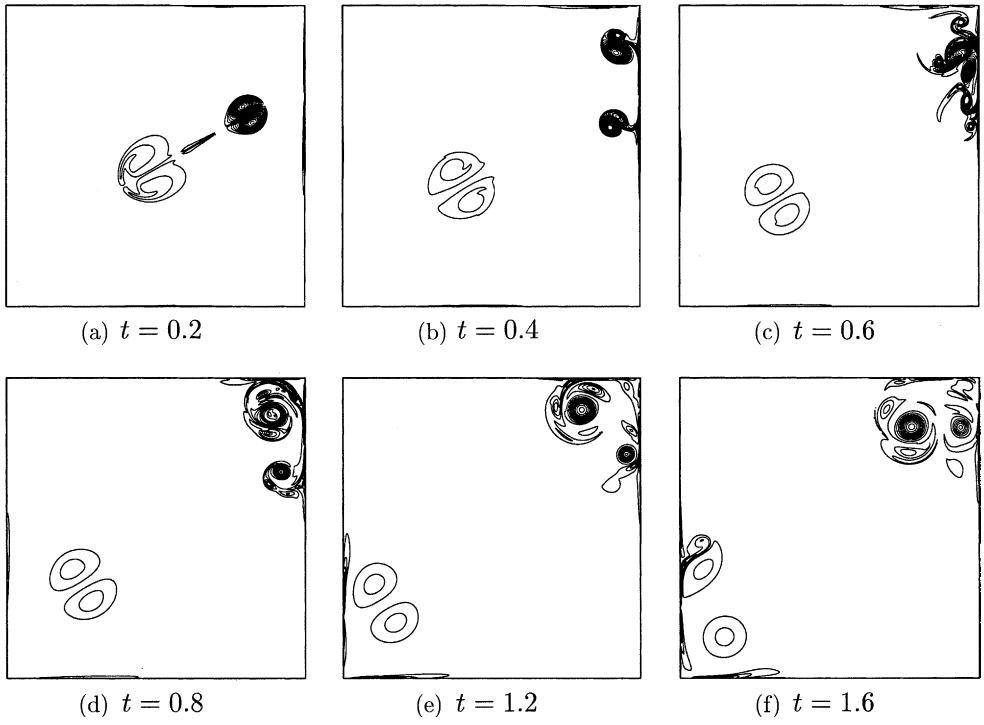

Fig. 10. Vorticity contour plots of the oblique dipole-wall collision experiment with $Re = 2500$. The pseudospectral simulations are performed with a resolution $N_{SM} = 640$. The contour levels are drawn for $\ldots, -50, -30, -10, 10, 30, 50, \ldots$ (representing dimensionless vorticity values).

at $t = 1$). Contour plots are only shown for the right top corner of the computational domain, i.e. $0 \leqslant x \leqslant 1$ and $0 \leqslant y \leqslant 1$. The solution for $Re = 5000$ is not the same with the two methods as the position of the secondary vortices around the positive primary vortex is different (compare the vortices and their locations in Figs. 12d and 13d).

The vorticity contour plot of the finite differences calculation with $Re = 1250$ shows minute differences with the pseudospectral computation (virtually no differences were observed for the global quantities like energy and enstrophy). The finite differences calculation with $Re = 1250$ should probably need a slightly larger resolution, $N_{FD} \approx 2200$, but with the available numerical algorithm we had to choose either $N_{FD} = 2048$ or 3072. Keeping in mind that our aim is not to decide which numerical method performs best, but to show how difficult it is to simulate a seemingly simple time-dependent flow problem and to provide well-resolved flow solutions, we concluded that for this purpose $N_{FD} = 2048$ is sufficient (whereas the spectral simulation with $N_{SM} = 384$ yields the well-resolved simulation).

In Fig. 15 we have plotted $E(t)$, $\Omega(t)$, and $P(t)$ for several runs with $Re = 2500$. The data are obtained from spectral simulations performed with 257, 385 and 513 Chebyshev polynomials per coordinate direction, and the curves displaying the time evolution for the energy and enstrophy for $N_{SM} = 384$ and 512 collapse onto one curve. Also for the oblique collision experiment the sharp decrease of the kinetic energy at $t \approx 0.32$ is due to the strong dissipation when the dipole collides with the boundary. The palinstrophy is an indicator for (small-scale) vorticity gradients

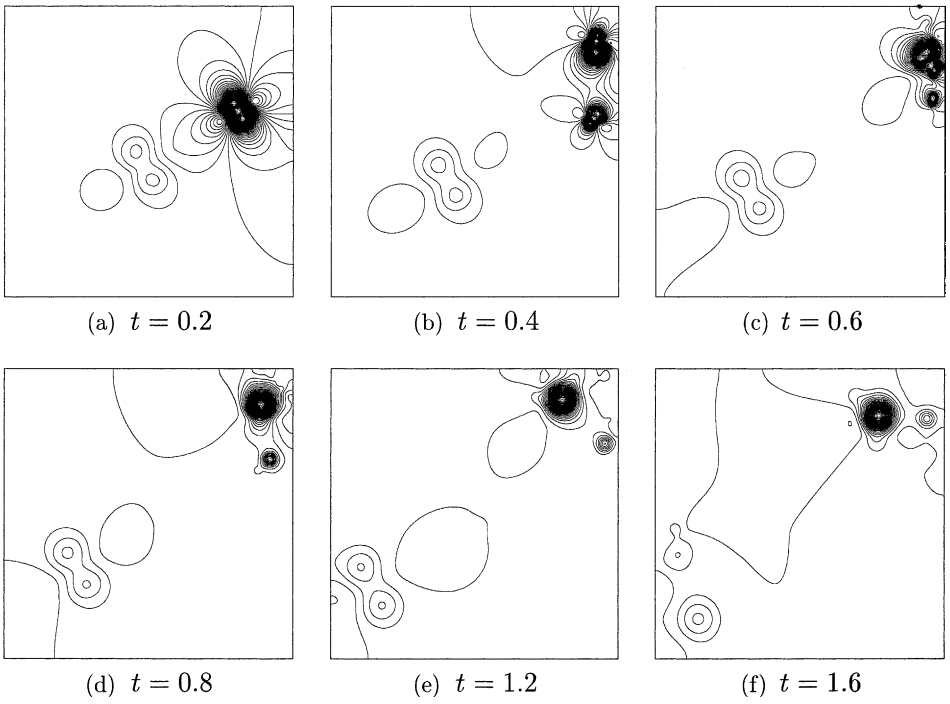

Fig. 11. Pressure contour plots of the oblique dipole-wall collision experiment with $Re = 2500$. The finite differences simulations are performed with a resolution $N_{FD} = 3072$. The contour levels are drawn for $\ldots, -3, -2, -1, 0, 1, 2, 3, \ldots$ and the contour line 0 goes through the origin of the domain.

which are abundant in the boundary layers and produced during the vortex–wall interaction, and requires a larger numerical effort to obtain mode-convergence for $P(t)$. However, the numerical data obtained for $P(t)$ in the run with $N_{SM} = 512$ is representative for the converged flow evolution and does not differ from the computation with $N_{SM} = 640$.

The use of the energy, enstrophy and palinstrophy to test the convergence of the flow evolution has one potential drawback: two seemingly similar curves, for instance the palinstrophy, might represent slightly different configurations of vorticity patches. As an alternative we have measured the total angular momentum L of the flow. This quantity, defined with respect to the origin of the container, has the following form:

$$L(t) = \int_{-1}^{1}\int_{-1}^{1}(xv(\mathbf{x},t) - yu(\mathbf{x},t))\,\mathrm{d}x\,\mathrm{d}y = -\frac{1}{2}\int_{-1}^{1}\int_{-1}^{1} r^2\omega(\mathbf{x},t)\,\mathrm{d}x\,\mathrm{d}y \tag{13}$$

with $r^2 = x^2 + y^2$. We have plotted the angular momentum L for the runs at $Re = 2500$ with the spectral method ($N_{SM} = 256$, 384, and 512, respectively) in Fig. 16a and we can conclude that the convergence of L is a delicate issue. The data obtained in a simulation with $N_{SM} = 512$ shows indeed mode-convergence, what is supported by a similar computation with the finite differences code with $N_{FD} = 3072$. The agreement of both methods is excellent (see Fig. 16b), and in our view our simulations fully capture the flow evolution of the dipole-wall collision experiment for $Re = 2500$.

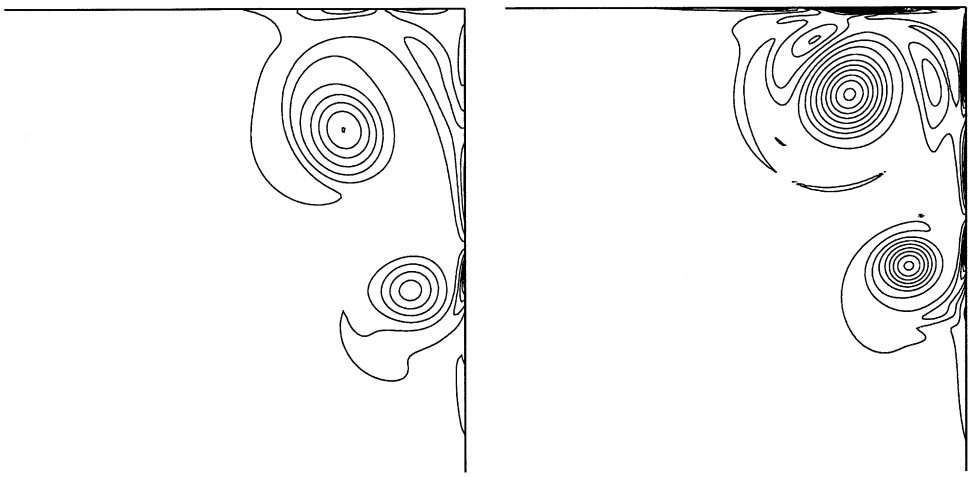

(a) $Re = 625$ $(N_{SM} = 256)$ (b) $Re = 1250$ $(N_{SM} = 384)$

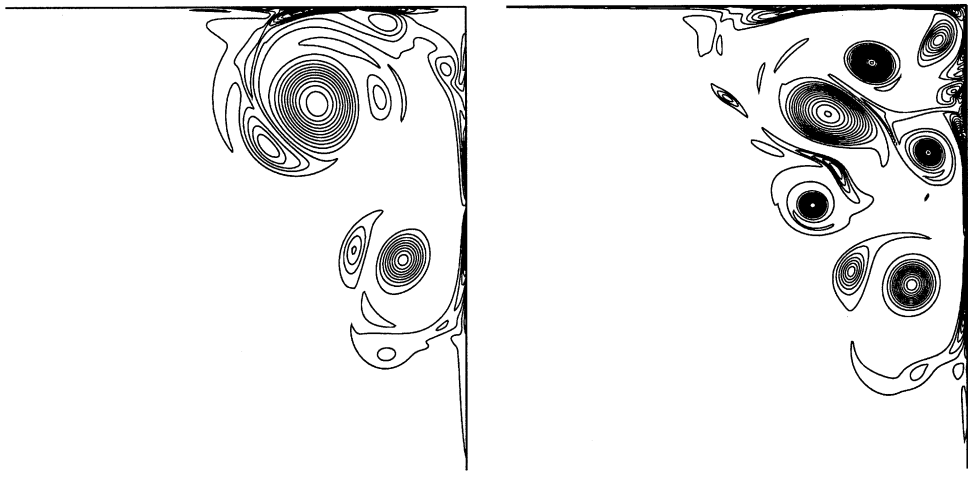

(c) $Re = 2500$ $(N_{SM} = 640)$ (d) $Re = 5000$ $(N_{SM} = 640)$

Fig. 12. Vorticity contour plots of the oblique dipole-wall collision experiment at $t = 1$ with $Re = 625$ (a), 1250 (b), 2500 (c), and 5000 (d). Only the right top part of the computational domain has been shown: $0 \leqslant x \leqslant 1$ and $0 \leqslant y \leqslant 1$. The pseudospectral simulations are performed with a resolution $N_{\mathrm{SM}} = 256$, 384, 640, and 640, respectively. The contour levels are drawn for $\ldots, -50, -30, -10, 10, 30, 50, \ldots$ (representing dimensionless vorticity values).

To support this statement we have collapsed the 2D Chebyshev spectra of the vorticity onto a 1D graph and inspect these spectra on exponential decay for large wave numbers. The following procedure has been carried out to compute the 1D spectrum of a function $f(x, y) = \sum_n \sum_m \hat{f}_{nm} T_n(x) T_m(y)$. We define the wave number $p = 1, 2, 3, \ldots, N_{\mathrm{SM}}$, the annular domains $\mathscr{P}_p$ with boundaries $\partial\mathscr{P}_{p,\mathrm{inner}} = p - \frac{1}{2}$ and $\partial\mathscr{P}_{p,\mathrm{outer}} = p + \frac{1}{2}$ and compute the spectrum $S_{\mathrm{f}}(p)$ according to

$$S_{\mathrm{f}}(p) = \frac{1}{P} \sum_{n,m \in \mathscr{P}_p} |\hat{f}_{nm}| \tag{14}$$

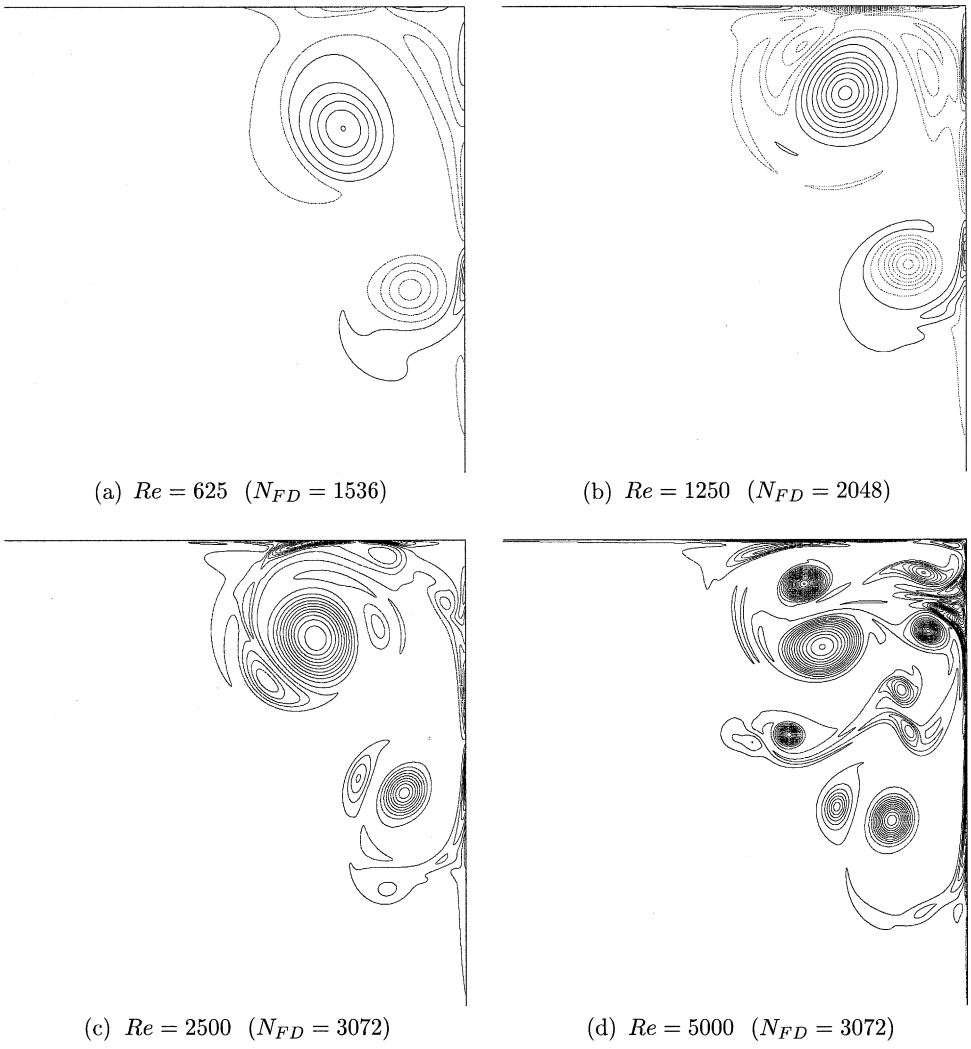

Fig. 13. Vorticity contour plots of the oblique dipole-wall collision experiment in the window $(0,1) \times (0,1)$ at $t = 1$ with $Re = 625$ (a), 1250 (b), 2500 (c), and 5000 (d). The finite differences simulations are performed with a resolution $N_{\mathrm{FD}} = 1536$, 2048, 3072, and 3072, respectively. The contour levels are drawn for $\ldots, -50, -30, -10, 10, 10, 30, 50, \ldots$ (representing dimensionless vorticity values).

with $P = \sum_{n,m \in \mathscr{P}_p}$ the number of Chebyshev wave numbers in the annular domain $\mathscr{P}_p$. In Fig. 17 we have plotted $S_\omega(p)$ for runs with $Re = 2500$ and $N_{\mathrm{SM}} = 384$, 512, and 640. The spectra are obtained for the vorticity fields at $t = 0.4$ and $t = 1.0$. The different spectra are virtually on top of each other for a wide range of wave numbers, and an increase of N_{SM} affects the highest wave number range only. These spectra show power-law decay of the intermediate wave number expansion coefficients and a clear exponential decay of high wave number expansion coefficients indicating well-resolvedness of the flow. The difference in slope for the spectra at $t = 0.4$ and $t = 1.0$ is most likely attributed to the different dominant flow phenomena represented by both

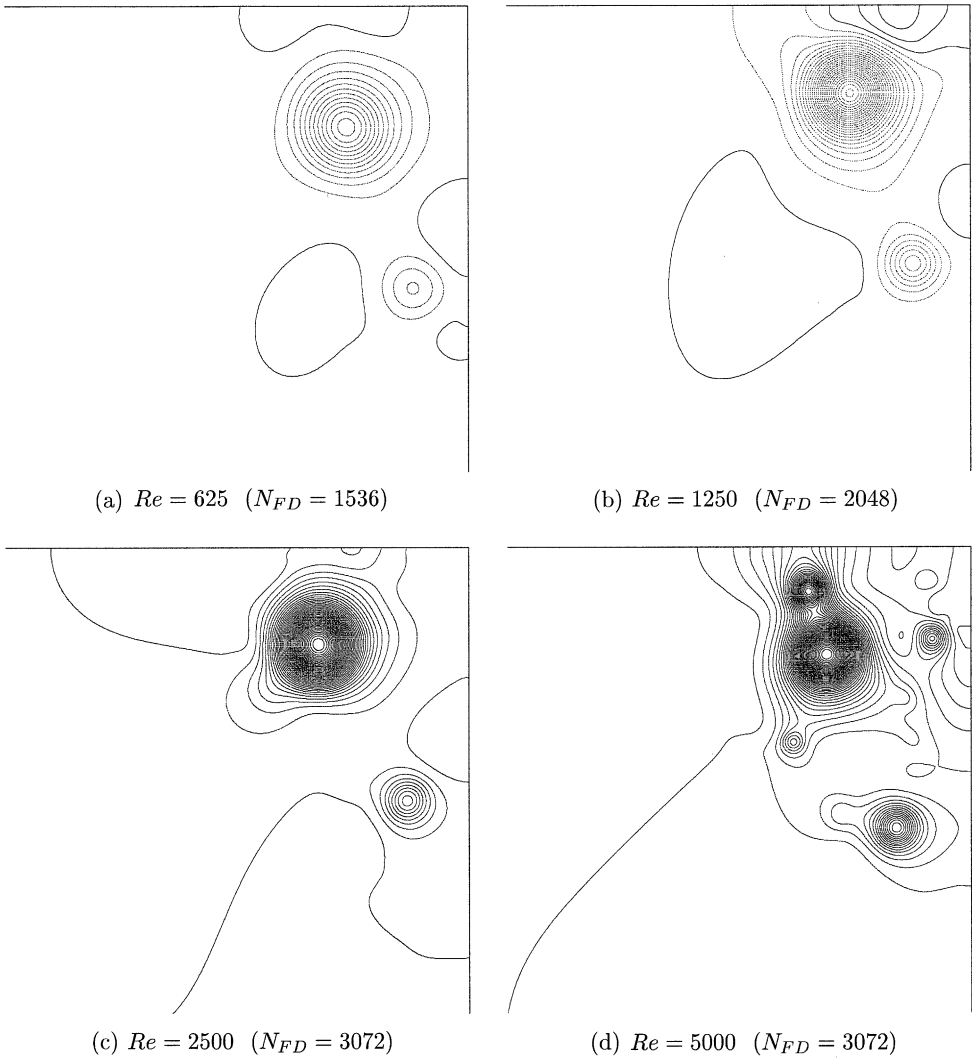

(a) $Re = 625$ $(N_{FD} = 1536)$ (b) $Re = 1250$ $(N_{FD} = 2048)$

(c) $Re = 2500$ $(N_{FD} = 3072)$ (d) $Re = 5000$ $(N_{FD} = 3072)$

Fig. 14. Pressure contour plots of the oblique dipole-wall collision experiment in the window $(0,1) \times (0,1)$ at $t = 1$ with $Re = 625$ (a), 1250 (b), 2500 (c), and 5000 (d). The finite difference simulations are performed with a resolution $N_{\mathrm{FD}} = 1536$, 2048, 3072, and 3072, respectively. The contour levels are drawn for $\ldots, -3, -2, -1, 0, 1, 2, 3, \ldots$ and the contour line 0 goes through the origin of the domain.

vorticity spectra. At $t = 0.4$ the violent vortex–wall interaction produces many small-scale vortices and vorticity filaments and the inverse energy cascade is assumed to be the dominant process in the energy spectrum (note that Eq. (14) does not represent the energy spectrum itself, thus reporting precise power laws are meaningless). At later times the flow is more or less dominated by decay processes and a direct enstrophy cascade will dominate the kinetic energy spectrum (see, for instance, Refs. [24,25]). We assume that these differences in power-law behaviour of the inertial range of the energy spectrum might also be reflected in the vorticity spectrum as defined by Eq. (14), which seems to be the case.

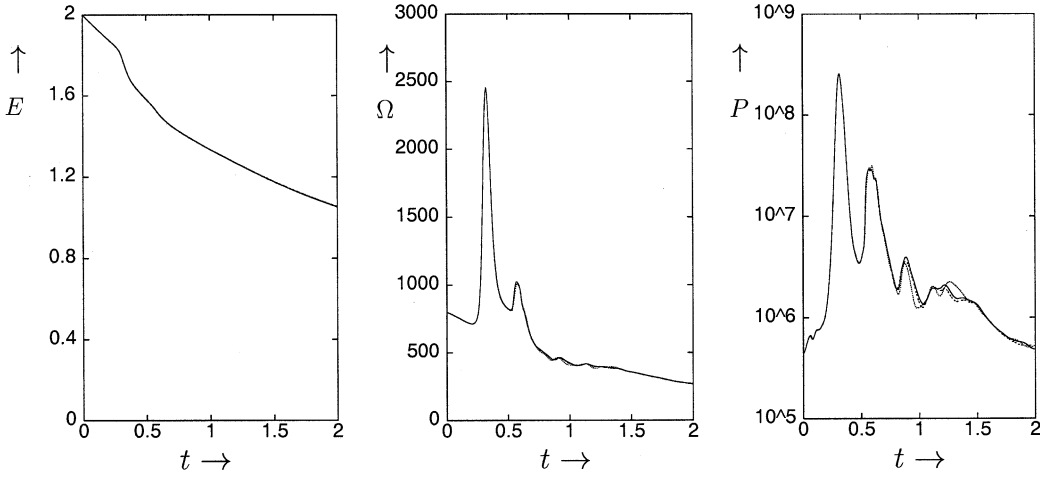

Fig. 15. From left to right: (a) the kinetic energy $E(t)$, (b) the enstrophy $\Omega(t)$, and (c) the palinstrophy $P(t)$ for the oblique dipole-wall collision with $Re = 2500$ and different resolutions $N_{SM} = 256$ (dotted), $N_{SM} = 384$ (dashed), and $N_{SM} = 512$ (solid) of the pseudospectral simulations.

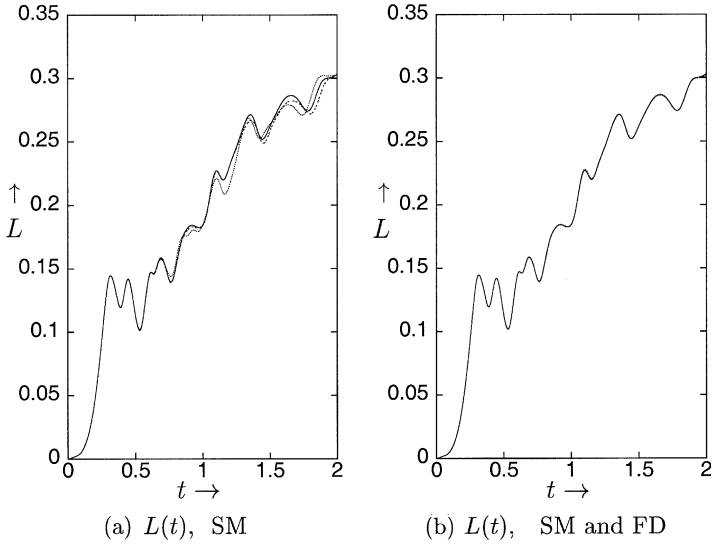

Fig. 16. The angular momentum for the oblique-wall collision with $Re = 2500$. The left panel shows the angular momentum obtained with the pseudospectral method and three different resolution: $N_{SM} = 256$ (dotted), 384 (dashed), and 512 (solid). The right panel shows the same quantity obtained with the pseudospectral ($N_{SM} = 512$) and the finite differences ($N_{FD} = 3072$) methods. These data are indistinguishable from each other.

Exponential convergence of our spectral simulations has been checked for runs with $Re = 625$ (oblique collision) and 1250 (normal collision). For this purpose we have carried out for each Reynolds number a series of simulations with a fixed time step and computed E, Ω, and P at

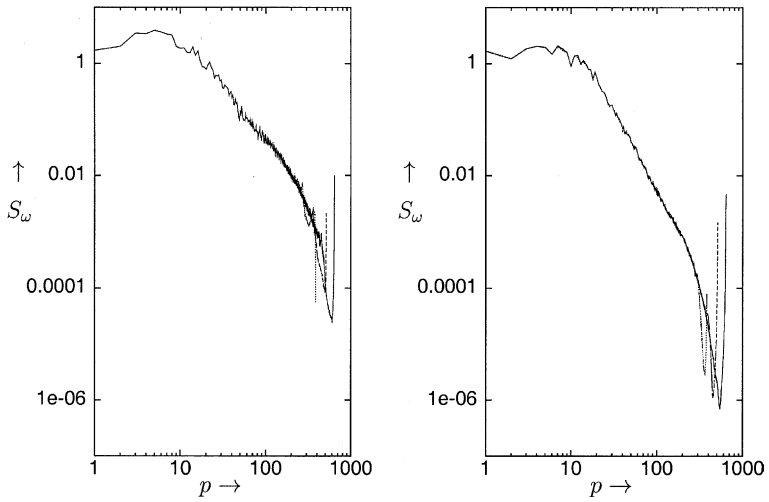

Fig. 17. The 1D Chebyshev spectra $S_\omega(p)$ from the oblique dipole-wall collision experiment with $Re = 2500$. The left and right panel display the spectra at $t = 0.4$ and $t = 1.0$, respectively, for simulations with $N_{SM} = 384$ (dotted), $N_{SM} = 512$ (dashed), and $N_{SM} = 640$ (solid).

$t = 0.4$ just after maximum vorticity and vorticity gradient production at the no-slip walls. For this series of simulations we used a higher maximum resolution than apparent from Table 1, $N_{SM,max} = 384$ for $Re = 625$ and $N_{SM,max} = 512$ for $Re = 1250$. The fixed time step used in these tests was: $\Delta t = 3.33 \times 10^{-5}$ for $Re = 625$ and $\Delta t = 2.00 \times 10^{-5}$ for $Re = 1250$. In Fig. 18 we show a semi-logarithmic plot of the relative error $\epsilon_{ct} = |E(N_{SM}) - E(N_{SM,max})|/E(N_{SM,max})$ (and similar definitions for the relative errors of Ω and P). These estimated errors show indeed exponential decay for increasing resolution.

The agreement between the computational results from the SM and FD runs is also confirmed by a comparison of $\Omega(t)$ and $P(t)$ as shown in Fig. 19.

The slight differences observed for the palinstrophy is most likely due to the computation of the large vorticity gradients in the boundary layers, which is probably not well computed with the finite differences method (see remarks made in Section 4). This is also illustrated by Figs. 20 and 21 where the contour plots of the vorticity field and the pressure are displayed for three instants in time for the $Re = 2500$ simulations. We can see in particular that the pressure localizes the primary vortices, i.e. the vortices constituting the dipole before the collision (but more local pressure extrema might eventually be formed). The contour plots for $t = 1.0$ and 2.0 are on top of each other, consistent with the conclusions drawn on the basis of Figs. 16b and 19. However, it should be stated again what the price actually is, a spectral computation with 641×641 Chebyshev collocation points or a finite difference calculation with 3072×3072 grid cells that require several weeks of CPU time on a work station. Small differences between the SM and FD results are found in the vorticity contour plots displayed in Figs. 20c and 21c (at time $t = 3$). (See the discussion in Section 4 where similar discrepancies have been observed for the normal collision experiment with $Re = 5000$, but in that case for $t \gtrsim 0.75$.) This indicates that mode- or grid-convergence is not fully obtained yet, but we would like to emphasize that the data for $t \lesssim 2.6$ are not affected (in

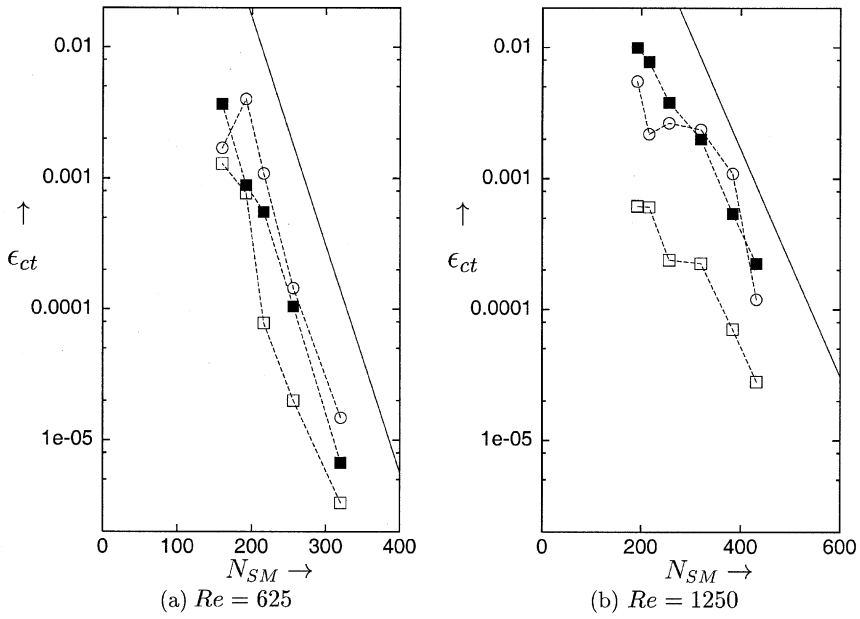

Fig. 18. The relative error $\epsilon_{ct} = |f(N_{SM}) - f(N_{SM,max})|/|f(N_{SM,max})$ of the energy ($f = E$, open square), enstrophy ($f = \Omega$, filled squares) and palinstrophy ($f = P$, open circles) of the flow field at $t = 0.4$ as a function of the resolution N_{SM}. $N_{SM,max} = 384$ for $Re = 625$ (oblique collision), and $N_{SM,max} = 512$ for $Re = 1250$ (normal collision). The solid lines represent exponential functions.

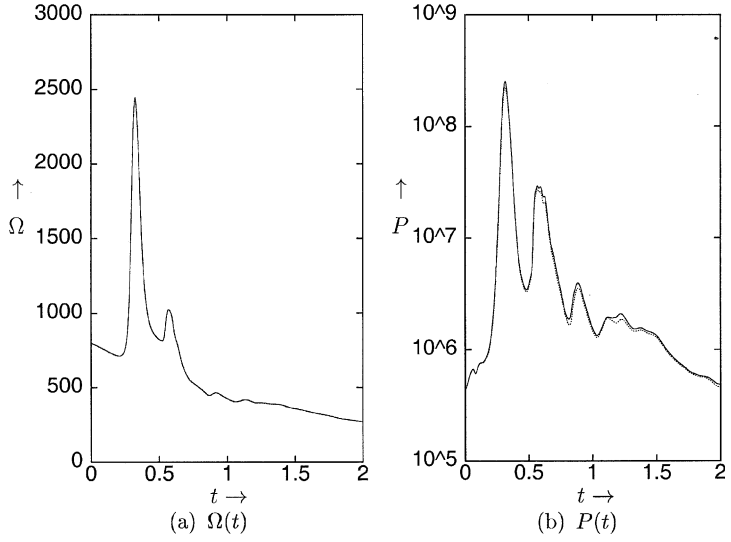

Fig. 19. The enstrophy (left) and palinstrophy (right) for the oblique dipole-wall collision at $Re = 2500$ obtained with the pseudospectral ($N_{SM} = 512$, solid line) and the finite differences ($N_{FD} = 3072$, dashed line) methods. The data for the enstrophy are indistinguishable from each other. The small discrepancies observed for the palinstrophy are discussed in the text.

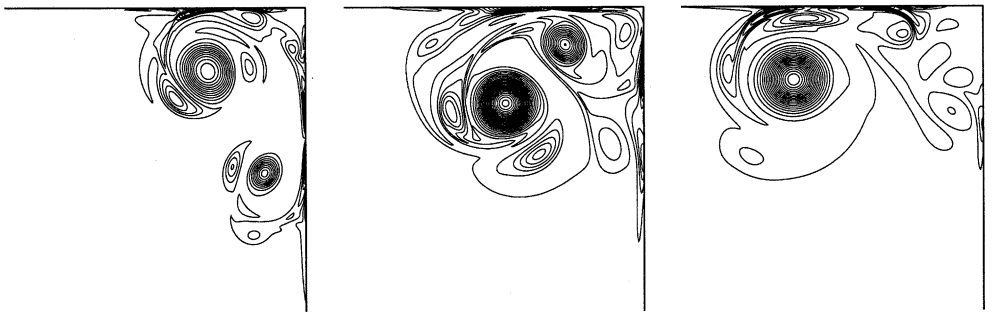

Fig. 20. Vorticity contour plots of the oblique dipole-wall collision experiment with $Re = 2500$ for $t = 1.0$, 2.0, and 3.0 computed with the pseudospectral method with $N_{SM} = 640$. Only the right top part of the computational domain has been shown: $0 \leqslant x \leqslant 1$ and $0 \leqslant y \leqslant 1$. The contour levels are drawn for $\ldots, -50, -30, -10, 10, 30, 50, \ldots$ (representing dimensionless vorticity values) for $t = 1.0$, and for $\ldots, -20, -12, -4, 4, 12, 20, \ldots$ for the other vorticity snapshots.

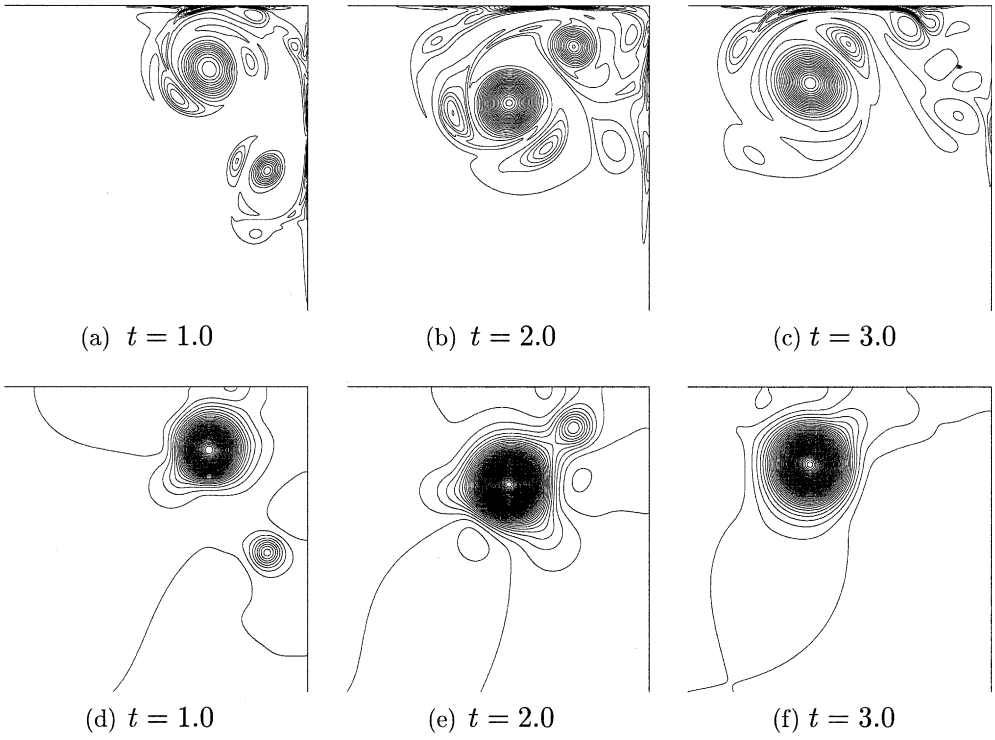

Fig. 21. Vorticity (top) and pressure (bottom) contour plots in the window $(0,1) \times (0,1)$ of the oblique dipole-wall collision experiment with $Re = 2500$ for $t = 1.0$, 2.0, and 3.0 computed with the finite differences method with $N_{FD} = 3072$. The vorticity contour levels are drawn for $\ldots, -50, -30, -10, 10, 30, 50, \ldots$ for $t = 1.0$, and for $\ldots, -20, -12, -4, 4, 12, 20, \ldots$ for the other times. The pressure contour levels are drawn for $\ldots, -3, -2, -1, 0, 1, 2, 3, \ldots$ for $t = 1.0$, and for $\ldots, -1.2, -0.8, -0.4, 0, 0.4, 0.8, 1.2, \ldots$ for the other times (the contour line 0 goes through the origin of the domain).

particular for the pseudospectral calculations). Finally, we have shown plots of $\Omega(t)$, $P(t)$, and $L(t)$ obtained by the pseudospectral and the finite differences computations for $Re = 625$, 1250, and 2500 until time $t = 2$ and $Re = 5000$ until time $t = 1$ in Fig. 22. The data are on top of each other, except for $Re = 5000$ and $t \gtrsim 0.75$.

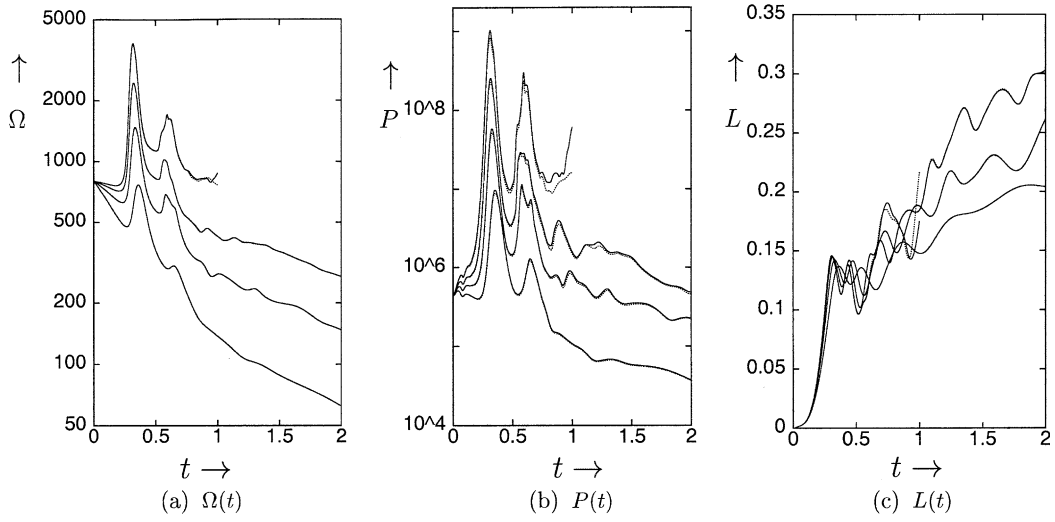

(a) $\Omega(t)$ (b) $P(t)$ (c) $L(t)$

Fig. 22. From left to right: $\Omega(t)$, $P(t)$ and $L(t)$ for $Re = 625$, 1250, 2500, and 5000 computed with the pseudospectral (solid lines) and the finite differences (dashed lines) method.

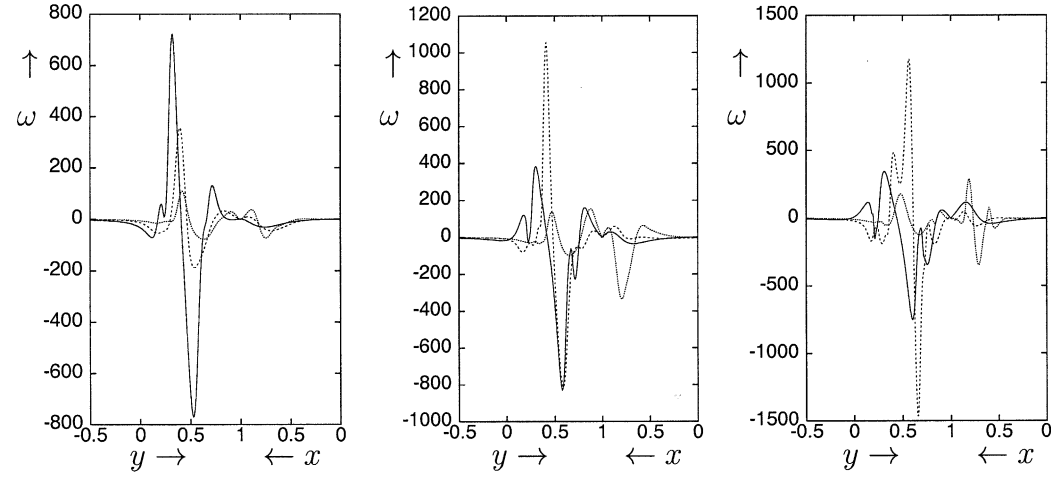

(a) $Re = 625$ (b) $Re = 1250$ (c) $Re = 2500$

Fig. 23. Vorticity at the boundary $x = 1$ (with $-0.5 \leqslant y \leqslant 1$) and $y = 1$ (with $0 \leqslant x \leqslant 1$) for $t = 0.4$ (solid), $t = 0.6$ (dashed) and $t = 1.0$ (dotted) for the oblique dipole-wall collision experiment from pseudospectral simulations. The resolution for the different runs is: (a) $N_{SM} = 256$, (b) $N_{SM} = 384$, and (c) $N_{SM} = 640$.

For the oblique collision experiment we have plotted in Figs. 23 and 24 the vorticity profiles and vorticity fluxes, respectively, at the boundary $x = 1$ ($-0.5 \leqslant y \leqslant 1$) and at the boundary $y = 1$ ($0 \leqslant x \leqslant 1$) for the runs with $Re = 625$ ($N_{SM} = 256$), 1250 ($N_{SM} = 384$), and 2500 ($N_{SM} = 640$). The data represent the vorticity at the boundary for $t = 0.4$ (solid), 0.6 (dashed) and 1.0 (dotted). Also for the oblique-collision case the vorticity distributions and the normal vorticity gradients at the boundaries are well-resolved; no changes were observed when the resolution was increased further.

In Tables 6 and 7 we have summarized the value of the first two maxima of the enstrophy and the palinstrophy, respectively, and the times at which the maxima occurs for the runs with

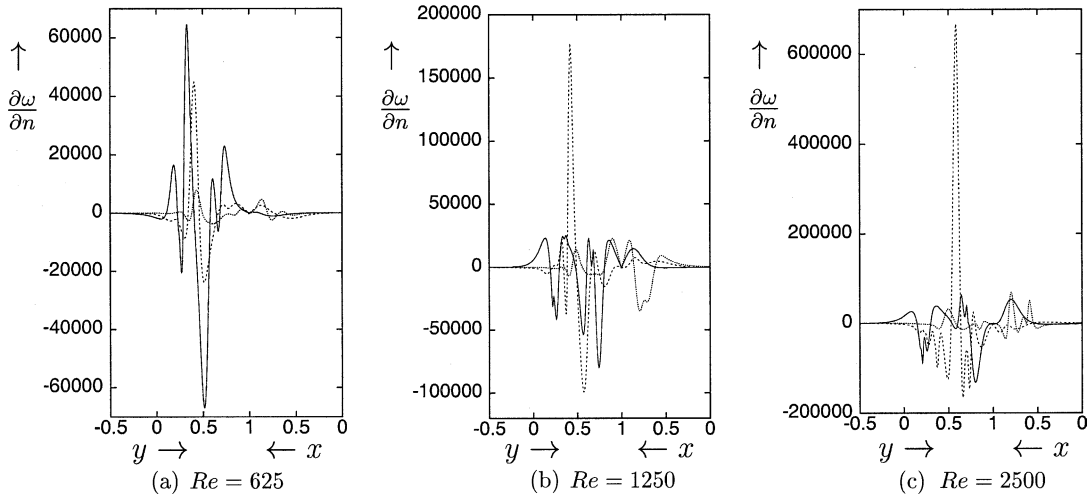

Fig. 24. Vorticity flux $\frac{\partial\omega}{\partial x}$ at the boundary $x = 1$ (with $-0.5 \leqslant y \leqslant 1$) and the vorticity flux $\frac{\partial\omega}{\partial y}$ at $y = 1$ (with $0 \leqslant x \leqslant 1$) for $t = 0.4$ (solid), $t = 0.6$ (dashed) and $t = 1.0$ (dotted) for the oblique dipole-wall collision experiment from pseudospectral simulations. The resolution for the different runs is: (a) $N_{SM} = 256$, (b) $N_{SM} = 384$, and (c) $N_{SM} = 640$.

Table 6
A summary of the values of the first two maxima of the enstrophy for the oblique collision experiment, which occur at t_1 and t_2, respectively

Re	Method	t_1	$\Omega(t_1)$	t_2	$\Omega(t_2)$
625	SM	0.3597	768.0	0.6441	304.5
	FD	0.360	766.6	0.6435	304.5
1250	SM	0.3351	1478	0.5819	688.8
	FD	0.335	1473	0.581	689.4
2500	SM	0.3230	2447	0.5692	1024
	FD	0.323	2435	0.569	1024
5000	SM	0.3173	3825	0.5936	1683
	FD	0.317	3769	0.591	1707

SM and FD denote spectral method and finite differences, respectively.

Table 7
A summary of the values of the first two maxima of the palinstrophy for the oblique collision experiment, which occur at t_1 and t_2, respectively

Re	Method	t_1	$P(t_1)$	t_2	$P(t_2)$
625	SM	0.3525	9.722×10^6	0.6471	1.290×10^6
	FD	0.353	8.887×10^6	0.6475	1.214×10^6
1250	SM	0.3261	5.797×10^7	0.5776	1.142×10^7
	FD	0.327	5.166×10^7	0.578	1.056×10^7
2500	SM	0.3150	2.545×10^8	0.5680	2.921×10^7
	FD	0.315	2.252×10^8	0.568	2.748×10^7
5000	SM	0.3111	1.029×10^9	0.5941	2.976×10^8
	FD	0.311	8.345×10^8	0.591	2.383×10^8

SM and FD denote spectral method and finite differences, respectively.

Re = 625, 1250, 2500, and 5000. These data are obtained from the well-resolved simulations based on the FD and SM computations (see Table 1).

The trajectories and vortex strengths $|\omega_{\max}|$ as well as the pressure at the core p_{FD} have been computed for the positive and negative primary vortices. The trajectories are shown in Fig. 25; the x-position of the vortices are shown in Fig. 25a (Re = 625 and 1250) and Fig. 25c (Re = 2500 and 5000). The open symbols denote the positive primary vortices, and the filled symbols represent the negative ones. Similarly, in Fig. 25b and d the y-position of the primary vortices is displayed. As can be seen in Fig. 25c and d, no reliable trajectories of the negative primary vortices could be identified for the simulation with Re = 5000, which is not a surprise keeping the vorticity contour plot of Fig. 12d in mind: a lot of vortical structures emerge, and we were not able to identify the remnants of the vortex of the original dipole with negative circulation. Moreover, the results for the position of the positive primary vortex could only be determined with sufficient accuracy up to $t \approx 1.2$. It is interesting to see that the trajectory of the positive vortex is only weakly influenced by the Reynolds number of the flow. This is slightly different for the negative primary vortex. For smaller Reynolds numbers (Re = 625 and 1250) the negative primary vortex is destroyed when it moves in between the positive primary vortex and the top wall, but for Re = 2500 it survives the passage between the dominant vortex with positive circulation and the no-slip boundary, and it subsequently moves like a satellite around the much stronger positive vortex.

We have also measured the maximum vorticity $|\omega_{\max}|$ of the positive and negative primary vortices in course of time. From these data it is obvious that the negative part of the dipole is more strongly affected by the no-slip wall, due to a stronger vortex–wall interaction, than its positive counterpart (see, for instance, Fig. 10). An interesting observation can be made for the vortex strength in the high Reynolds number runs. Consider the open and filled circles in Fig. 26. The decrease of the vorticity amplitude $\omega_{\max}$ of the positive vortex (open circles) suddenly decreases and behaves virtually linearly as function of time ($t \gtrsim 0.8$). This behaviour is absent for the runs with Re = 625 and 1250, where the decrease is approximately exponential. The contour plots shown in Fig. 10 indicate a possible mechanism: the positive vortex core is surrounded by small vortices and vorticity filaments with opposite sign of vorticity. This ring of opposite vorticity seems to shield the strong positive vortex core from the no-slip walls, thereby reducing the dissi-

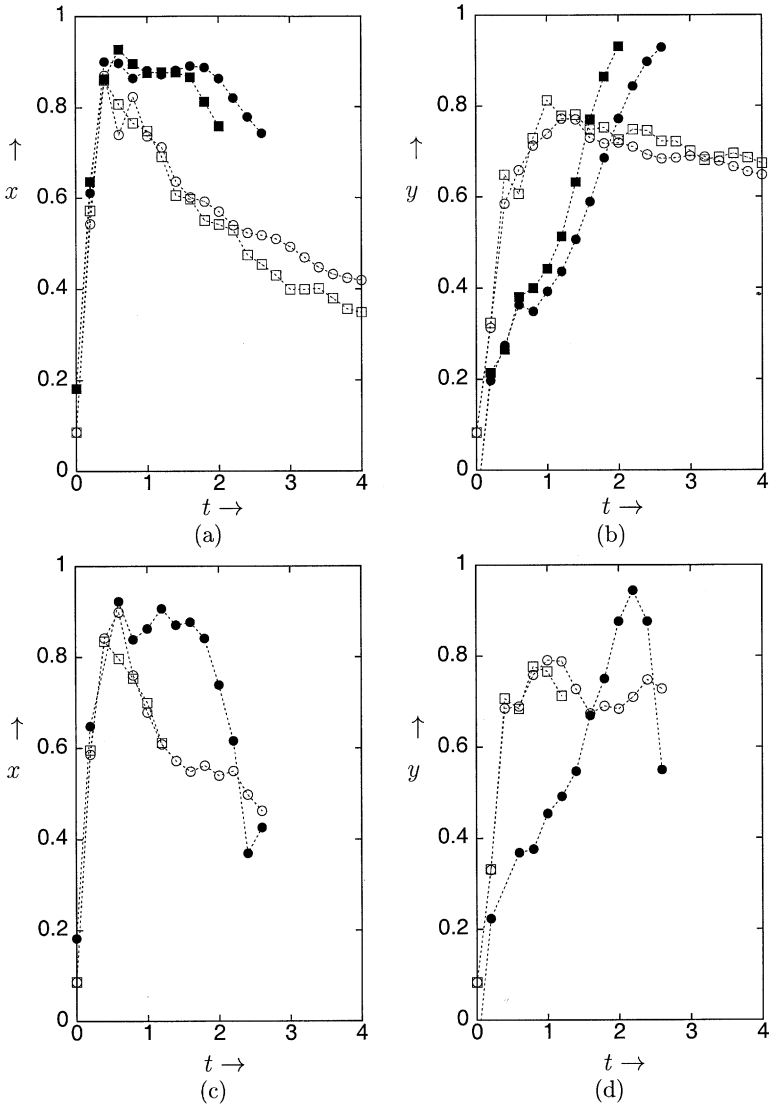

Fig. 25. The trajectory of the primary positive and negative vortices as function of time for the oblique collision experiment. The x- and y-position of the primary vortices is displayed for $Re = 625$ (circles) and 1250 (squares) in (a, b), respectively, and for $Re = 2500$ (circles) and 5000 (squares) in (c, d), respectively. The open symbols denote the positive primary vortices, and the filled symbols represent the negative primary vortices.

pation of the vortex. Another feature is given by the pressure p_{FD} at the core of the primary vortices (Fig. 27). We can see in particular that the evolution of the pressure for the positive primary vortex is slowed down and even reversed after the collisions.

In Tables 8 and 9 we have collected numerical data on primary vortex position, vortex strength ω_{max} and pressure at the core p_{FD} which might be used for benchmarking purposes. These data are obtained from the well-resolved simulations (highest values of N_{SM} and N_{FD} as indicated in Table 1). As already mentioned in Section 4, the pseudospectral runs with $Re = 5000$ are slightly

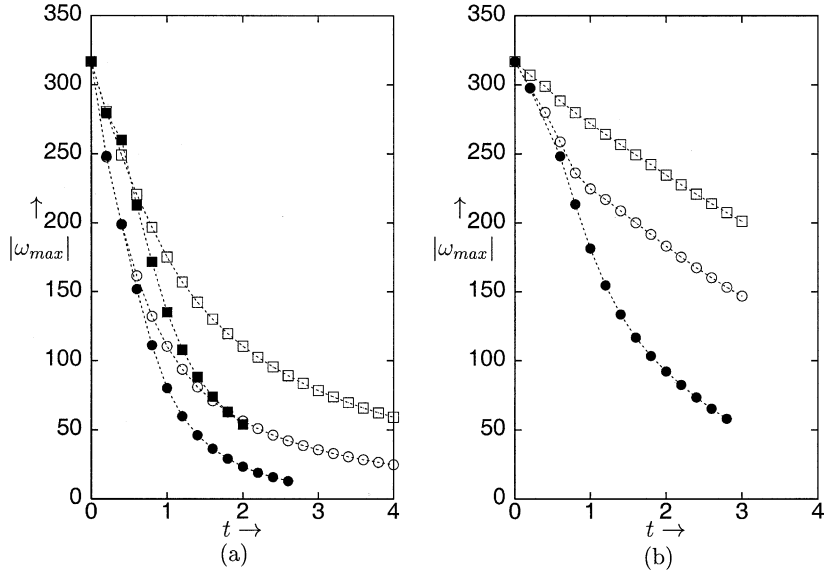

Fig. 26. The (absolute value of the) vortex amplitude $|\omega_{\max}|$ of the primary positive and negative vortices as function of time for the oblique collision experiment. The vortex amplitude of the primary vortices is displayed for $Re = 625$ (circles) and 1250 (squares) in (a), and for $Re = 2500$ (circles) and 5000 (squares) in (b). The open symbols denote the amplitude of the positive primary vortex, and the filled symbols represent the amplitude of the negative primary vortex.

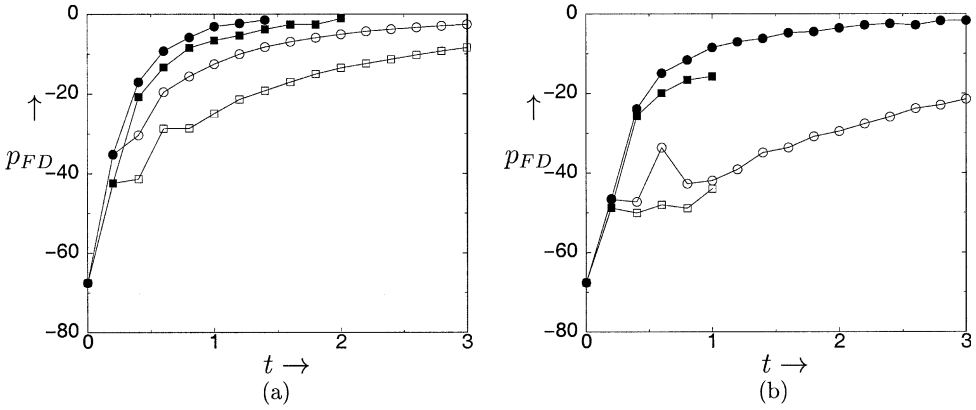

Fig. 27. The pressure p_{FD} at the core of the primary positive and negative vortices as function of time for the oblique collision experiment. The pressure of the primary vortices is displayed for $Re = 625$ (circles) and 1250 (squares) in (a), and for $Re = 2500$ (circles) and 5000 (squares) in (b). The open symbols denote the positive primary vortex, and the filled symbols represent the amplitude of the negative primary vortex.

contaminated by residual high-frequency oscillations. These are due to slight under-resolvedness of the details of the boundary layer formed during the first (and undoubtedly strongest) vortex–wall interaction, and affect accurate determination of the position and strength of the primary vortices (in particular for $t = 1.2$ in Tables 8 and 9). It appears that the oblique test requires more modes (SM) or points (FD) to fully converge.

Table 8
An overview of the x- and y-coordinate, the maximum strength ω_{max} and the pressure at this maximum of the positive primary vortex for four different times $t = 0.6$, 1.2, 1.8, and 2.4

Re	t	$(x,y)_{SM}$	$(x,y)_{FD}$	$\omega_{max,SM}$	$\omega_{max,FD}$	p_{FD}
625	0.6	(0.740, 0.659)	(0.740, 0.659)	161.5	161.4	−19.54
	1.2	(0.712, 0.772)	(0.711, 0.771)	93.80	93.74	−10.03
	1.8	(0.592, 0.717)	(0.591, 0.716)	63.0	63.0	−5.88
	2.4	(0.523, 0.693)	(0.523, 0.693)	46.2	46.2	−3.77
1250	0.6	(0.807, 0.607)	(0.807, 0.607)	220	220	−28.67
	1.2	(0.691, 0.779)	(0.691, 0.779)	157.0	157.0	−21.40
	1.8	(0.550, 0.753)	(0.551, 0.754)	119.7	119.6	−15.04
	2.4	(0.475, 0.745)	(0.477, 0.746)	95.52	95.44	−11.31
2500	0.6	(0.899, 0.689)	(0.900, 0.690)	258.7	258.7	−33.60
	1.2	(0.608, 0.788)	(0.609, 0.789)	217.0	216.6	−39.10
	1.8	(0.560, 0.691)	(0.555, 0.694)	191.6	191.2	−30.80
	2.4	(0.499, 0.743)	(0.500, 0.734)	167.5	167.2	−25.89
5000	0.6	(0.797, 0.684)	(0.794, 0.680)	288	288	−48.02
	1.2	(0.612, 0.712)	(0.643, 0.710)	264	264	−43.05

SM and FD indicate spectral method and finite differences, respectively (the pressure is shifted so that $p = 0$ at the origin of the domain).

Table 9
An overview of the x- and y-coordinate, the maximum strength ω_{max} and the pressure at this maximum of the negative primary vortex for four different times $t = 0.6$, 1.2, 1.8, and 2.4

Re	t	$(x,y)_{SM}$	$(x,y)_{FD}$	$\omega_{max,SM}$	$\omega_{max,FD}$	p_{FD}
625	0.6	(0.898, 0.364)	(0.898, 0.365)	−151.9	−151.8	−9.26
	1.2	(0.872, 0.436)	(0.872, 0.435)	−59.9	−59.9	−2.28
	1.8	(0.887, 0.685)	(0.888, 0.685)	−29.1	−29.2	−0.62
	2.4	(0.778, 0.898)	(0.779, 0.896)	−15.8	−15.8	−0.23
1250	0.6	(0.928, 0.381)	(0.928, 0.381)	−212.7	−212.5	−13.41
	1.2	(0.877, 0.513)	(0.877, 0.514)	−108.0	−108.3	−5.34
	1.8	(0.812, 0.865)	(0.811, 0.867)	−63.00	−63.16	−2.60
2500	0.6	(0.923, 0.368)	(0.923, 0.368)	−248.3	−248.2	−14.94
	1.2	(0.907, 0.492)	(0.906, 0.484)	−154.9	−155.1	−7.06
	1.8	(0.841, 0.746)	(0.841, 0.738)	−103.7	−104.0	−4.46
	2.4	(0.40, 0.90)	(0.448, 0.928)	−73.9	−74.5	−2.50
5000	0.6	(0.894, 0.319)	(0.892, 0.320)	−278	−278	−19.89
	1.2	–	(0.909, 0.470)	–	−224	−12.83

SM and FD indicate spectral method and finite differences, respectively (the pressure is shifted so that $p = 0$ at the origin of the domain).

6. Discussion and conclusions

We have presented numerical experiments on normal and oblique dipole-wall collisions. This study was not primarily aimed at investigating the dynamics of dipoles colliding with a no-slip wall,

but to provide some, at least in our view, reliable data that might be used to test numerical algorithms. This study originated from 2D turbulence simulations on bounded domains where it was found that the impact of the presence of a no-slip wall has serious consequences for the evolution of 2D turbulence. Moreover, a detailed study on the enstrophy and palinstrophy production by dipoles colliding with no-slip walls (with Reynolds numbers up to 1.6×10^5) revealed the necessity of an extremely high resolution of the flow near the boundaries to capture the collision process as accurate as possible. This could be achieved reasonably well, although the dynamics of the produced and remaining vortices could not be predicted very well. In this study we focussed therefore on the relatively low Reynolds number case ($Re \leqslant 5000$). We used a finite differences and a pseudospectral code for the flow simulation and determined the minimum necessary number of grid cells or Chebyshev collocation points to capture the flow dynamics as accurate as possible. This minimum number turned out to be extremely large, at least much larger than expected by us. For example, the two low Reynolds number examples required at least 257 ($Re = 625$) and 385 ($Re = 1250$) Chebyshev modes per coordinate direction in the pseudospectral simulations and 1536^2 and 2048^2 grid cells, respectively, in the finite differences simulations to obtain converged results up to $t = 6$.

The required resolution for mode- or grid-convergence turned out to be consistent. Consider, for example, the convergence for the oblique dipole-wall collision with $Re \leqslant 2500$ up to $t \approx 2.6$. We needed 257, 385, and 513 Chebyshev polynomials (per coordinate direction) for the pseudospectral runs with $Re = 625$, 1250, and 2500, respectively, and 1536, 2048, and 3072 grid cells per coordinate direction for the finite differences simulations. This is consistent with the boundary layer thickness which is proportional to $1/\sqrt{Re}$.

We expect that the present results might be useful as a benchmark for testing different numerical algorithms. It concerns simple flow problems, with well-defined initial conditions, in a flow domain with a simple geometry bounded by no-slip walls. This test case might thus be very suitable for simulations with vortex methods (see, e.g., Refs. [4,5,7]), penalisation techniques [8,9], wavelets [26,27], immersed boundary methods [10] and adaptive schemes.

Acknowledgments

One of us (H.J.H.C.) is grateful for the financial support by Université Bordeaux 1 for visits to the Applied Mathematics Department of Bordeaux University where substantial part of this work has been conducted. This work was sponsored by the Stichting Nationale Computerfaciliteiten (National Computing Facilities Foundation, NCF) for the use of supercomputer facilities, with financial support from the Netherlands Organization for Scientific Research (NWO).

References

[1] Clercx HJH, Nielsen AH. Vortex statistics for turbulence in a container with rigid boundaries. Phys Rev Lett 2000;85:752–5.
[2] Clercx HJH, van Heijst GJF. Dissipation of kinetic energy in two-dimensional bounded flows. Phys Rev E 2002;65:066305 (1–4).
[3] Orlandi P. Vortex dipole rebound from a wall. Phys Fluids A 1990;2:1429–36.

[4] Ould-Salihi ML, Cottet G-H, El Hamraoui M. Blending finite-difference and vortex methods for incompressible flow computations. SIAM J Sci Comput 2000;22:1655–74.
[5] Cottet G-H, Koumoutsakos P, Ould Salihi ML. Spatially varying cores for viscous vortex methods. J Comput Phys 2000;162:164–85.
[6] Kravchenko AG, Moin P, Moser R. Zonal embedded grids for numerical simulations of wall-bounded turbulent flows. J Comput Phys 1996;127:412–23.
[7] Cottet G-H, Koumoutsakos P. Vortex methods: Theory and practice. Cambridge, UK: Cambridge University Press; 2000.
[8] Angot Ph, Bruneau Ch-H, Fabrie P. A penalization method to take into account obstacles in an incompressible flow. Numer Math 1999;81:497–520.
[9] Kevlahan NK, Ghidaglia JM. Computation of turbulent flow past an array of cylinders using a spectral method with Brinkman penalization. Eur J Mech B/Fluids 2001;20:333–50.
[10] Fadlun EA, Verzicco R, Orlandi P, Mohd-Yusof J. Combined immersed-boundary/finite-difference methods for three-dimensional complex flow simulations. J Comput Phys 2000;161:35–60.
[11] Bruneau Ch-H, Saad M. The 2D lid-driven cavity problem revisited. Comput Fluids, in press doi:10.1016/j.compfluid.2004.12.004.
[12] Bruneau Ch-H, Jouron C. An efficient scheme for solving steady incompressible Navier–Stokes equations. J Comput Phys 1990;89:389–413.
[13] Clercx HJH. A spectral solver for the Navier–Stokes equations in the velocity-vorticity formulation for flows with two non-periodic directions. J Comput Phys 1997;137:186–211.
[14] Daube O. Resolution of the 2D Navier–Stokes equations in velocity-vorticity form by means of an influence matrix technique. J Comput Phys 1992;103:402–14.
[15] Orszag SA. Numerical methods for the simulation of turbulence. Phys Fluids 1969;12(Suppl II):250–7.
[16] Canuto C, Hussaini MY, Quarteroni A, Zang TA. Spectral methods in fluid dynamics. Berlin: Springer-Verlag; 1987.
[17] Lamb H. Hydrodynamics. Cambridge, UK: Cambridge University Press; 1932.
[18] Coutsias EA, Lynov JP. Fundamental interactions of vortical structures with boundary layers in two-dimensional flows. Physica D 1991;51:482–97.
[19] Ersoy S, Walker JDA. Flow induced at a wall by a vortex pair. AIAA J 1986;24:1597–605.
[20] Coutsias EA, Lynov JP, Nielsen AH, Nielsen M, Juul Rasmussen J, Stenum B. Vortex dipoles colliding with curved walls. In: Christiansen PL, et al., editors. Future directions of nonlinear dynamics in physical and biological systems. New York: Plenum Press; 1993. p. 51–4.
[21] Verzicco R, Flór JB, van Heijst GJF, Orlandi P. Numerical and experimental study of the interaction between a vortex dipole and a circular cylinder. Exp Fluids 1995;18:153–63.
[22] Bruneau Ch-H. On the large-Reynolds-number 2D dipole-wall collision benchmark. In: Proceedings of BAIL2002, Perth, Australia, 2002, p. 55–60.
[23] Kravchenko AG, Moin P, Shariff K. B-spline method and zonal grids for simulations of complex turbulent flows. J Comput Phys 1999;151:757–89.
[24] Clercx HJH, van Heijst GJF. Energy spectra for decaying two-dimensional turbulence in a bounded domain. Phys Rev Lett 2000;85:306–9.
[25] Wells MG, Clercx HJH, van Heijst GJF. Vortices in oscillating spin-up. J Fluid Mech, submitted for publication.
[26] Schneider K, Farge M. Coherent vortex simulation of an impulsively started cylinder at $Re = 3000$ using an adaptive wavelet method with penalisation. In: Castro IP, Hancock PE, Thomas TG, editors. Advances in turbulence IX. Barcelona: CIMNE; 2002. p. 471–4.
[27] Schneider K, Paget-Goy M, Pellegrino G, Verga A, Farge M. Direct numerical simulation of an impulsively started, or uniformly accelerated, plate using adaptive wavelet and Fourier methods with penalisation. In: Proceedings of the Third International Symposium on Turbulence and Shear Flow Phenomena, Sendai, Japan, 2003. p. 407–12.